Chapter 2
Experimental Setup and Techniques

Most of the experiments presented in this thesis have been performed on the Vienna atom chip setup internally labeled as "Rb2". The current setup has been developed in Heidelberg starting from 2002 and moved, rebuilt and extended in Vienna from 2006. The first section will be devoted to a brief description of the apparatus. The second section will focus on the techniques used to create, control and characterize magnetic double-well potentials on our atom chip setup. The last section will present the imaging systems used to probe the atoms.

2.1 Experimental Setup

As in most BEC experiments, a different atomic sample (a cold thermal cloud or a Bose-Einstein condensate) is prepared at each experimental cycle, before it is manipulated and eventually released and destructively imaged. A Magneto Optical Trap (MOT) is used to trap Rubidium atoms from the background gas. The atoms are optically cooled down by an optical molasses an then optically pumped and confined in a magnetic Ioffe-Pritchard-type trap created by a macroscopic copper structures behind the atom chip. After a first step of radio-frequency evaporative cooling, the atoms are transferred into the actual chip trap and further cooled down. Eventually, the condensate is released from the trap and imaged in time of flight (tof), either by an absorption or a fluorescence imaging system. Each experimental cycle of the Rb2 machine lasts about 37 s, including 18 s in the MOT and 10 s of cooling and trapping in the the two magnetic traps. The aim of this section is to present the main steps of the experimental cycle and the hardware used to realize them. Figure 2.1 shows an overview of the Rb2 setup.

The status of the experiment, as presented in this thesis, shows little difference to that described in the previous theses of the students who worked on the experiment, in particular the Ph.D. thesis of Bücker [1] (2013). The following sections will briefly recapitulate the most important features of our setup, with emphasis on the techniques

T. Berrada, *Interferometry with Interacting Bose-Einstein Condensates in a Double-Well Potential*, Springer Theses,
DOI 10.1007/978-3-319-27233-7_2

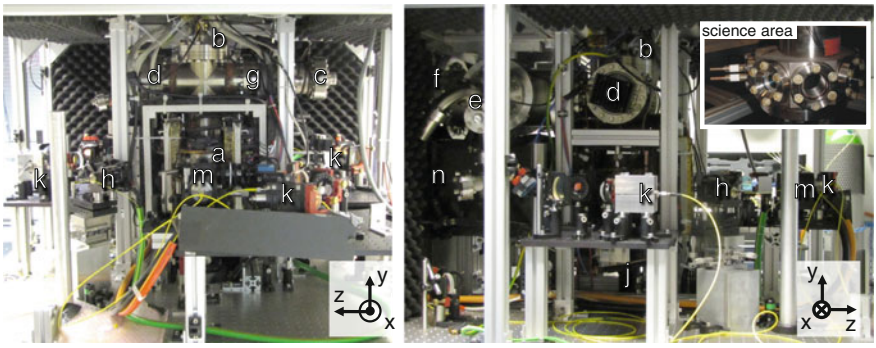

Fig. 2.1 Overview pictures of the Rb2 setup. Adapted from Ref. [1]. *Left* front view, *right* side view. **a** Science area, surrounded by Helmholtz coil pairs, **b** Chip mounting flange, **c** Ti-sublimation pump, **d** LIAD viewport, **e** Cluster flange with vacuum valve and ion gauge, **f** (behind panel) Ion getter pump, **g** NEG pump, **h** Light sheet illumination optics, **j** Light sheet objective (facing upwards), **k** Various fiber couplers for optical pumping beams, **m** Fiber coupler for absorption imaging, **n** (behind panel) Absorption imaging camera. *Inset* science area (*octagon*) with viewports and dispenser current feedthrough (*left*)

used in the experiments presented in this thesis. More specific information can be found in the Ph.D. and diploma theses of the students who worked on the Rb2 experiment in Heidelberg and Vienna, as well as in the publications of the Rb2 team:

- initial design and general aspects of atom chip experiments: Krüger [2], Wildermuth [3], Gimpel [4], Becker [5], Haupt [6] and Hofferberth [7]
- radio-frequency dressed potentials, in particular double wells: Schumm [8], Hofferberth [9], Betz [10] and Refs. [11–14]
- chip manufacturing and characterization: Groth [15], Manz [16] and Ref. [17]
- upgrades performed after the move to Vienna: Manz [16], Betz [10], Bücker [1, 18]
- imaging systems: Bücker [1, 18] and Refs. [19–21].
- micro-wave and radio-frequency systems: Koller [22], Plisson [23].
- experiment control: Bradjic [24], Rohringer [25] and Ref. [26]

2.1.1 Vacuum Chamber and Rubidium Source

The experiments take place in a single stainless steel ultrahigh vacuum chamber. It contains the atom chip and its mounting, which is suspended by a large vacuum flange at the top of the vessel. The vacuum pumps (an ion pump,[1] a passive non-evaporative getter pump[2] and a Titanium sublimation pump (TSP), the filaments of which are

[1] Varian StarCell, 500 L/s.

[2] SAES Getters.

heated every few weeks) are mounted in the chamber on dedicated flanges. The chip is located in the lower half of the chamber and is surrounded by an octagonal vessel equipped with anti-reflection coated viewports ($\geq$1 in. clear aperture diameter) on seven of its faces, providing optical access for the MOT, optical pumping and imaging beams, as well as the Rubidium dispensers on the eighth face. Another dispenser is placed directly behind a viewport to be used as a Light Induced Desorption source (LIAD, not implemented yet). The bottom flange is a large viewport used for two of the MOT beams as well as the fluorescence imaging.

On the one hand, experiments with BECs require a low background pressure (of the order of 10^{-11} mbars) to ensure a good lifetime, but on the other hand, a background pressure of 10^{-9} mbars is necessary to load the MOT from the ambient Rb vapor. This means that the pressure changes by two order of magnitude during each experimental cycle. This is achieved by pulsing the current in the dispensers for about 17 s at the beginning of each cycle to desorb gaseous Rb. The MOT is held for another $\sim$1.5 s with dispenser off to allow the pumps to capture the remaining hot background gas before the rest of the cooling sequence starts.

2.1.2 External Coils

Coils

Uniform magnetic fields are required throughout the sequence. They are created by six pairs of coils located outside the vacuum chamber. For each spatial direction, each of the two pairs is operated close to Helmholtz configuration to produce a homogeneous magnetic field close to the center, but with opposite orientation, labeled as *Big and Small Bias field* in the horizontal x direction, *Big and Small Ioffe field* in the horizontal z direction and *Big and Small Up-Down field* in the vertical y direction (see Fig. 2.1 for the orientation of the axes). For each direction, one pair of coils is made of thick copper wires (*Big*-) to create fields up to tens[3] of Gauss, while the other pair (*Small*-) is made of thinner wires to provide smaller fields of a few G. This configuration with two sets of coils is advantageous when changes in field magnitude and direction are needed on a timescale which cannot be met by the current sources. It also allows using unipolar current supplies and matching the current and voltage ranges to the requirements of each coil.

Current Sources

The current sources[4] are operated in current-stabilized mode to output a constant current and avoid long-term thermal drift. The current target is set by an analog control voltage from the sequencer. The only exception is the offset field providing

[3]Fields magnitude larger than 100 G should be achievable but not required in the current experimental cyclee.

[4]HP/Agilent 65xx series, excepted for the small Up-Down field, where a bipolar supply (High-Finesse BCS-5/5) is used.

the trap bottom in the final chip trap (small Ioffe field, see Sect. 2.2.1.2). In particular for extremely cold samples obtained by radio-frequency evaporative cooling close to the trap bottom, the stability of the small Ioffe field determines the reproducibility of the BEC production. It is also crucial for the stability of the dressed double wells, because fluctuations of the small Ioffe field translate into fluctuations of the RF dressing detuning (see Sect. 2.2.2.2), and hence of the shape of the potential. Particularly in the kHz regime (of the order of the transverse trapping frequency), noise at the mG level has to be suppressed, because it would result in a technical heating of the BEC.

To take advantage of the fact that the supply for the small Ioffe turns out to be less noisy in controlled-voltage mode, it is voltage-stabilized on a 1 Ω precision resistor[5] (temperature coefficient < 1 ppm/K) connected in series with the coil, yielding a relative current stability better than 10^{-5} at 0.5 G. Details of the small Ioffe stabilization setup and noise characteristics can be found in Bücker's Ph.D. thesis [1].

Switches

Fast switching (<0.1 ms) is achieved using home-made field-effect transistor (FET) switches to stand currents up to 60 A and induced voltages uo to 400 V. Still, the coils switches are among the devices which break more frequently on the experiment.

2.1.3 Chip Mounting and Copper Structure

The chip mounting (see Fig. 2.2a) hangs upside down in the vacuum chamber so that the atoms can levitate below the chip surface (see Fig. 2.2b), allowing to perform tof measurements. The chip mounting consists of 10 copper rods and ceramic spacers, as well as "macroscopic" copper wires (∼1 mm thickness) embedded in a ceramic block ensuring electrical insulation as well as heat conductivity. These copper wires form an additional layer of current carrying structures approx. 1 mm behind the chip surface in order to produce non-homogenous magnetic fields (see Fig. 2.2c):

- a broad **H-shaped structure**, electrically connected as a U wire, is used together with the big Bias field and the big Up-Down field to create the MOT quadrupole approximately 1 cm below the chip surface, in a region where the MOT beams intersect [5, 27, 28]. In contrast to the standard MOT configuration with three pairs of counterpropagating beams, the mirror MOT is created by replacing two beams by reflection of the beams impinging on the surface of the atom chip, tilting the beam configuration by 45° with respect to the chip surface [28]. Scanning the magnitude of the two external fields allows changing the position of the MOT as well as the orientation of the quadrupole axes, in order to match the beam configuration. It is often necessary to optimize iteratively these parameters, for

[5] Isabellenhütte RUG-Z.

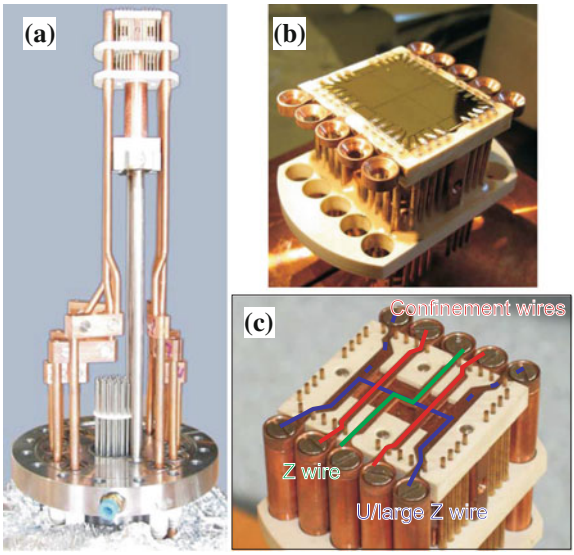

Fig. 2.2 The atom chip and its mounting. Adapted from Ref. [1]. **a** Chip mounting. At the *bottom*, the vacuum flange with feedthroughs for high-current copper rods and chip wires is seen. The steel tube in the center can be used for water cooling. Near the *top*, the copper rods and chip connection pins are guided by a ceramic (Shapal) block. When mounted, the copper structrue hangs upside down. **b** Atom chip, glued to ceramic mounting block. Near the edges of the atom chip, bond wires between connection pins and pads on the chip are seen. **c** Copper structures underneath the atom chip. Z-, U- and outer confinement wires are traced in *green*, *blue*, and *red*, respectively

example to ensure that the MOT is not located in the shadow of one of the chip wire.

Besides, the copper U is also used as a radio-frequency antenna for evaporative cooling.

- a **Z-shaped wire** is used together with the big Bias field and the small Ioffe field to create a Ioffe-Pritchard magnetic trap [27, 29, 30]. After the molasses phase, the atoms are optically pumped into the magnetically trappable state $F = 1, m_F = -1$ (see Sect. 2.2.1.1) and transferred into the Z trap located a few mm below the chip surface, where the RF evaporative cooling starts.
- any of the two **I shaped wires** perpendicular to the long axis of the chip trap can be used to create a longitudinal gradient for Stern and Gerlach separation of the magnetic spin states during tof (see Sect. 3.2).

The copper mounting is connected to the top vacuum flange which is equipped with electrical high current feedthroughs (up to 60 A) for the macroscopic copper wires, as well as pins for the Kapton wires connected to the atom chip ($I \leq 1$ A).

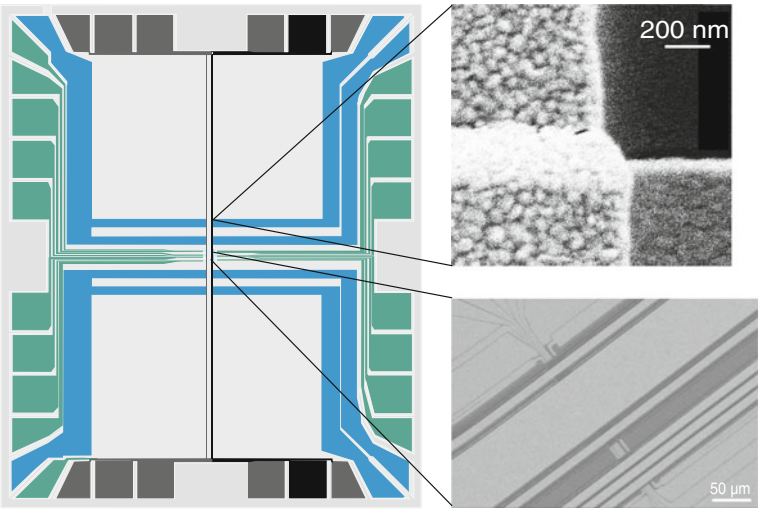

Fig. 2.3 Layout and of the Rb2 chip. Adapted from Ref. [16]. *Left* The *blue* and *green* wires (perpendicular to the long axis of the trap) belong to the first layer (deepest with respect to the chip surface). The *black* and *gray* wires (parallel to the long axis of the trap) belong to the second layer (closest to the surface). The *light gray* area is coated with gold as well, and serves as a mirror for the MOT beams. *Top Right* Wire in the second layer climbing up an insulation pad. *Bottom right* electron microscope image of the central part of the chip showing six wires in the second layer, in particular the main trapping wire (80 µm wide) and the two wires used for the RF dressing (10 µm wide) (Color figure online)

2.1.4 Atom Chip

The chip currently used on the Rb2 setup has been designed and manufactured by Groth in the group of I. Bar-Joseph at the Weizmann institute [17]. Details of the manufacturing can be found in Ref. [17] and in the Ph.D. thesis of Groth [15], characterization in the Ph.D. thesis of Manz [16]. It consists of a double-layer gold surface on a silicon substrate (see Fig. 2.3). The current-carrying structures are gold wires on two levels separated by an insulating layer to allow wire crossings. The rest of the surface is coated with gold and serves as a mirror for the MOT. A simplified sketch of the layout can be found in Sect. 2.2.

Currents up to 1 A (depending on the wires) are sent through connection pads placed all around the chip, excepted in the middle of each edge to ensure good optical access. Each pad is bonded with a copper pin connected to an electrical feedthrough on the base flange. The atom chip is directly glued onto the mounting. The heat produced by current flowing in the microwires is evacuated through the substrate into the mounting, which is water cooled.

Despite insulation pads at the position of the wire crossing, it turned out that some of the wires were electrically in contact. To avoid current leaks, the current driver for each wire is floating and connected to an independent set of car batteries (± 12 V) to supply the wire and the current source. Great care has to be taken to avoid grounding of the wire. In the long run, the heat dissipated by the microwires slightly bends

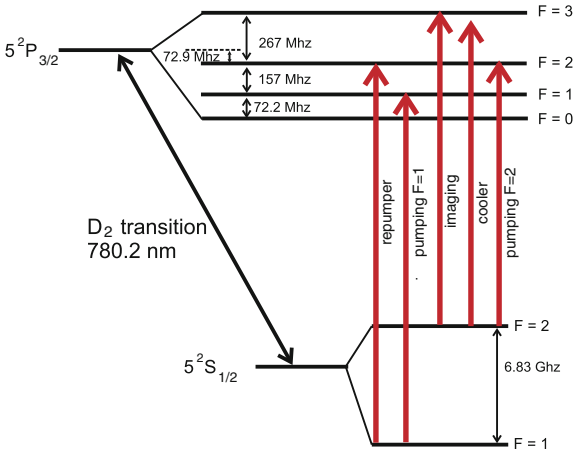

Fig. 2.4 Hyperfine structure and lasers. Adapted from Ref. [1]. Hyperfine structure of the D2 line of Rubidium 87 and laser frequencies used on the experiment

the chip surface, which affects the position of the mirror MOT and the molasses. To operate the experiment in steady state, current is always sent in the wires during the same amount of time at each experimental cycle, implying a buffer time at the end of the sequence. When used continuously, the car batteries have to be reloaded every week.

2.1.5 Optics and Laser System

Lasers are used for the MOT, repumping, optical pumping and imaging of the atoms (see Fig. 2.4). One laser source is used for each of the transitions between the two hyperfine states $F = 1$ and 2 of the ^{87}Rb electronic ground state ($5^2S_{1/2}$) and the excited state $5^2P_{3/2}$ (D2 line). Their wavelength is approximately 780.2 nm (the frequencies of the lasers differ by $\nu \approx 6.85$ GHz). Both lasers are external-cavity diode lasers (ECDL). Each is locked on the corresponding line (or crossover line) of a Rb vapor in a cell at room temperature through a Doppler-free saturated spectroscopy scheme (the description of a locking system similar to the one used on our experiment can be found in the diploma thesis of Wilzbach [31]). The structure of the laser system is sketched on Fig. 2.5.

Cooler Laser

The cooler laser[6] is mounted in a Master Oscillator Power Amplifier (MOPA) configuration. The Tappered Amplifier (TA) produces up to 1 W optical power which is launched into a single-mode, polarization-maintaining (SMPM) fiber. About 90 % of the optical power at the output of the fiber is transferred to a second fiber which outputs about 240 mW. Most of it is used for imaging, allowing to tune the intensity of

[6]Toptical Photonics TA100.

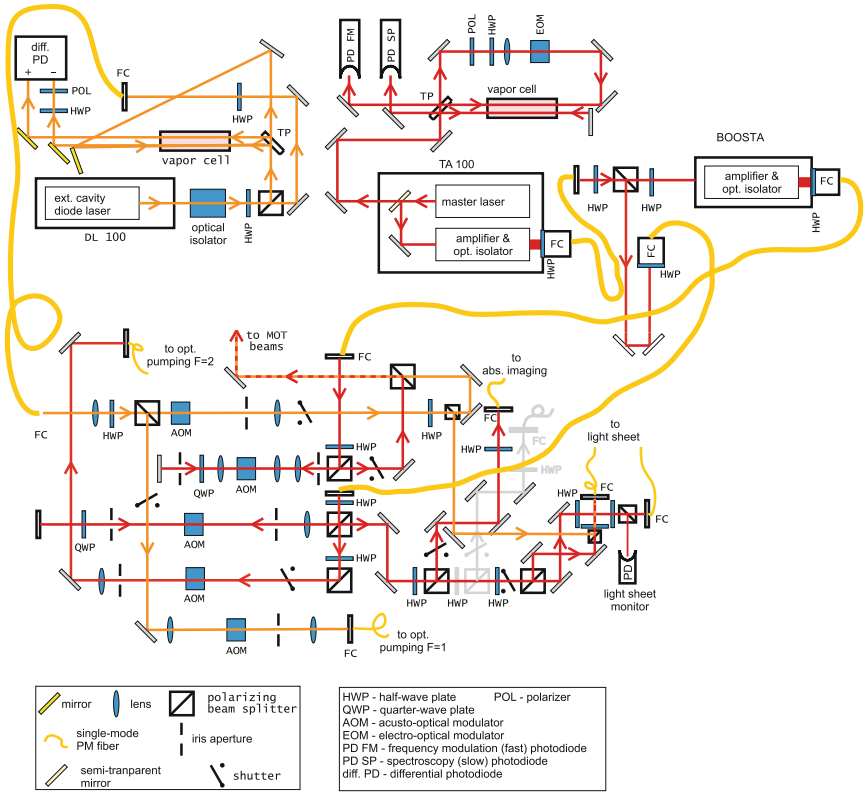

Fig. 2.5 Laser setup. Updated from Ref. [1]. *Red* and *orange lines* indicate F = 2 (cooler) and F = 1 (repumper) beam paths, respectively. The *greyed-out* parts belong to the former longitudinal imaging, which is not in use currently. The *upper part* of the drawing shows the laser spectroscopy setups for the F = 1 (*left*) and F = 2 (*right*) lasers, which are placed in a separate box to provide better thermal and acoustic isolation from the environment. The F = 2 laser uses a dual spectroscopy setup to simultaneously provide a normal Doppler-free spectroscopy and an additional path for Pound-Drever-Hall locking using an electro-optical modulator (EOM) for sideband modulation. Both lasers are coupled into single-mode polarization-maintaining fibers and brought to the BOOSTA amplifier (*right*) and to the AOM and beam distribution setup shown in the *lower part*. Finally the beams are guided to their destinations by free-field beam lines (MOT) or single-mode fibers (imaging, optical pumping)

the absorption imaging system up to 8 times the saturation intensity (see Sect. 2.3.1). The rest (a few mW) is used to drive the transition[7] $F = 2,\ F' = 2$. It has been used in the past to optically pump atoms into the magnetically trapped ($F = 2, m_F = 2$) state. Currently, since we trap the atoms in ($F = 1, m_F = -1$), we only employ this line to "repump" atoms from the $F = 2$ state into $F = 1$ after the molasse phase,

[7]The notation $F = n$ denotes a hyperfine state of the ground state while $F' = m$ denotes a hyperfine state of the excited state.

before optically pumping them with the $F = 1 \leftrightarrow F' = 1$ transition. The remaining output power of the TA (∼40 mW) is used to seed a second laser amplifier,[8] which is also coupled to a SMPM fiber (about 600 mW available optical power at the output of the fiber). It is used exclusively for the MOT beams.

Repumper

Since repumping and optical pumping on the other hand do not require large intensities, the repumper[9] consists of a single ECDL coupled into a SMPM fibre, yielding an output power of 40 mW. It is used for standard repumping during the MOT + molasse phase as well as to bring the atoms into the imaging transition. A small fraction of the light is used for the optical pumping into $(F = 1, m_F = -1)$.

Frequency Shifting

The hyperfine splittings in the excited state of ^{87}Rb are small enough (tens of MHz) to be addressed by Acousto-Optical Modulators (AOM) downstream in the beam paths (see Fig. 2.5) and in the same time large enough to be well-resolved. The cooler (MOT + molasses) beams, the detuning of which need to be dynamically changed during the cycle, as well as the imaging beam, are frequency-shifted by a double-pass AOMs. Typical detunings (with respect to the $F = 2 \leftrightarrow F' = 3$ transition) lie between −15 MHz (MOT) and −70 MHz (molasse). The other beams are sent through single-pass AOMs and are frequency shifted by a fixed amount to be resonant with the corresponding transitions.

2.1.6 Radio-Frequency Evaporative Cooling

Radio-Frequency Cooling Electronics

The radio-frequency (rf) source used for evaporative cooling is a digital arbitrary waveform generator.[10] The rf field frequency has to range from several MHz down to the Larmor frequency at the center of the trap (typically a few hundred kHz). This is achieved in Direct Digital Synthesizer (DDS) mode by concatenating waveforms consisting of a single period of a cosine wave at different frequencies spanning the desired range. This way, no phase jump occurs, but the frequency changes by discrete steps. The size of the frequency steps is chosen to decrease exponentially as the frequency approaches the trap bottom. While loading all the wave forms into the memory of the signal generator can take several minutes, the instruction sequence sent at each experimental sequence only contains the order of the basic waveforms and the number of times they have to be looped, and can be uploaded in a few s, during the MOT loading phase. This way, arbitrary frequency ramps can be produced and optimized in order to improve the cooling process.

[8] Toptica Photonics BoosTA.

[9] Toptica Photonics DL100.

[10] Tabor Electronics, WonderWave Series.

The rf field is radiated onto the atoms through the macroscopic copper U-wire on the chip mounting (see Fig. 2.2c). The waveform generator produces a constant-amplitude voltage and is not current-stabilized.

Cooling Sequence

Forced rf evaporative cooling starts after the atoms have been optically pumped to the ($F = 1, m_F = -1$) state and loaded into the Z trap. After the first ramp (3 s), the Z trap is compressed and brought closer to the chip. Approximately 2 million atoms at $T \sim 50$ mK are transferred into the chip trap. Further evaporation is performed in the chip trap for another 3 s, before the chip trap is compressed and brought to its final position ~60 μm below the surface of the chip. A final evaporation ramp (2 s) is performed to reach degeneracy and produce a Bose-Einstein condensate with typically a few thousand atoms.

Other Oscillating Fields

Note that besides rf evaporative cooling, time-varying magnetic fields in the kHz to GHz frequency range are used on the Rb2 setup for rf dressing of the potential (~900 kHz), controlled displacement of the trap (~3 kHz) and addressing of the ground state hyperfine transition (6.834 GHz). While the rf dressing electronics will be addressed in detail in Sect. 2.2.2, a description of the electronics for the trap position modulation ("shaking") can be found in Bücker's Ph.D. thesis [1] and Refs. [32, 33]. A description and a characterization of the rf/microwave setup which has been used in particular to address the *clock states* $F = 1, m_F = -1$ and $F = 2, m_F = 1$ can be found in Koller's Ph.D. thesis [22] and in Plisson's Master thesis [23].

2.1.7 Computer Control and Acquisition

The sequencer[11] is the spinal cord of the experiment. It is a stand-alone, real-time computer controlling 32 analog voltage channels (16 bits, ±10 V) and 64 digital Transistor-Transistor Logic (TTL) channels (0–5 V) used a triggers. The whole experimental cycle is coded as a matrix describing a sequence of values for each channel—in a similar fashion as a musical score [34]—with a minimal time step size of 25 μs. The sequence is transmitted from a dedicated computer through an link at the beginning of each cycle. Programming the sequence occurs through a Matlab interface which is also used to address devices which are not controlled by the sequencer, including the imaging cameras and the rf sources. The acquisition also relies on a Matlab interface for the read-out of analog control probes,[12] the read-out and the storage of camera pictures and the real time preprocessing of the data. Informations are exchanged between the computers (currently 6 different computers + the sequencer) through a local network by shared Windows drives and TCP/UDP connections.

[11] Jäger ADwin Pro.

[12] National Instruments USB-6218.

2.2 Trapping Atoms Magnetically with an Atom Chip

In this section, we will present the techniques used to trap atoms with magnetic fields on our atom chip setup. In particular, we will describe how the technique of rf dressing can be employed to create a tunable double-well potential.

2.2.1 Magnetic Trapping with Static Fields

2.2.1.1 Magnetic Trapping of Neutral Atoms

Magnetic trapping of neutral atoms relies on the local interaction between the magnetic field and the magnetic moment of the atoms. When the magnetic field is sufficiently weak so that the Zeeman shift is small compared to the hyperfine splitting (see Ref. [35] for the ^{87}Rb data), the total angular momentum $\vec{F}$ is a good quantum number to describe the coupling of an atom to the field and the interaction Hamiltonian reads

$$H = \vec{\mu}_F \cdot \vec{B}. \tag{2.1}$$

In the ^{87}Rb ground state ($5^2S_{1/2}$), the hyperfine splitting between $F = 1$ and $F = 2$ is approximately 6.8 GHz. For typical magnetic fields of a few G, the Zeeman shift is of the order of a few MHz. Furthermore, if the Larmor angular frequency $\omega_{\mathrm{L}} = g_{\mathrm{F}}\mu_{\mathrm{B}}|\vec{B}|/h$, where μ_{B} is the Bohr magneton, is large compared to the rate at which the field probed by the atoms changes

$$|\partial\vec{B}/\partial t| < \omega_{\mathrm{L}}|\vec{B}|, \tag{2.2}$$

the magnetic moment aligns adiabatically to the local magnetic field, so that the interaction takes the form of a potential

$$V_{\mathrm{mag}}(\vec{r}) = m_{\mathrm{F}} g_{\mathrm{F}} \mu_{\mathrm{B}} |\vec{B}(\vec{r})|. \tag{2.3}$$

In the $F = 1$ hyperfine state, the Landé factor $g_{\mathrm{F}} \approx -1/2$. Since Wing's theorem forbids the existence of a local field maximum in free space [36], the only Zeeman substate of $F = 1$ which can be trapped is $m_{\mathrm{F}} = -1$. The conversion factor between potential energy and field magnitude is $\kappa \equiv |g_{\mathrm{F}}|\,\mu_{\mathrm{B}} = h \times 0.7$ MHz/G. Note that atoms in $F = 2$, $m_{\mathrm{F}} = 1, 2$ can also be trapped. The choice of $F = 1$ on the Rb2 setup was partly motivated by observations showing that the three-body loss rate in a BEC was higher for $F = 2$ [37, 38]. Experiments coupling the two *clock states* ($F = 1$, $m_{\mathrm{F}} = -1$; $F = 2$, $m_{\mathrm{F}} = 1$), which experience the same potential, with a two-photon (microwave + rf) transition were also performed on the Rb2 setup [23].

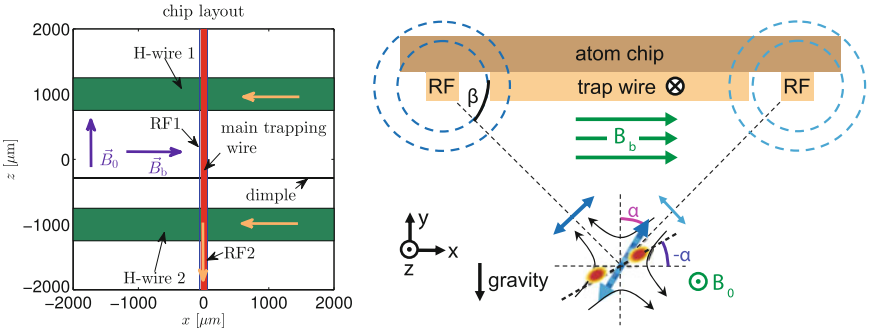

Fig. 2.6 Chip wires layout and schematics. *Left* Layout of the chip wires (at scale). *Red* main trapping wire (width: 80 μm), flanked by the two RF wires (*blue*, width: 10 μm). *Green* the two H-wires responsible for the longitudinal confinement (width: 500 μm). The dimple wire (width: 18 μm), located at 290 μm from the origin, can be used to locally deform the longitudinal potential for measurements of ω_z. The *orange arrows* indicate the orientation of the DC currents. The *purple arrows* indicate the orientation of the uniform external fields. The trap is located close to the origin. The typical length (in the z direction) of a BEC is 50 μm. The height of the wires (in y direction) is about 1 μm. *Right* Schematics of the configuration to create a double well. The DC current in the main trapping wire, together with the Bias field $\vec{B}_b$, creates a magnetic quadrupole ∼60 μm below the chip. The external Ioffe field $\vec{B}_0$ completes the Ioffe-Pritchard configuration. AC currents in the two RF wires located at 55 μm on each side of the main trapping wire create a linearly polarized RF field. Its orientation (angle α) can be tuned by changing the current balance and the relative phase between the RF wires. They produce a tunable double well oriented along an axis tilted by the angle $-\alpha$ with respect to the horizontal direction (*red spots*)

For an atom oscillating in a trap at the angular frequency $\omega_\perp$ (amplitude of the order of $a_\perp = \sqrt{\hbar/m\omega_\perp}$) around the potential minimum characterized by the Larmor angular frequency ω_L, the adiabaticity criterion (2.2) imposes $\omega_\perp \ll \omega_L$.

2.2.1.2 Static Trap

A few years after the first demonstration of atom trapping with a free-standing wire [39], microfabricated structures were developed to trap atoms [40, 41], before Bose-Einstein condensation on an atom chip was achieved in 2001 [42, 43]. Atom chips can produce strong confinements in the vicinity of the current carrying microstructures, while offering a high degree of control and robustness. Besides the review by Folman et al. [27], the book edited by Reichel and Vuletic [44] gives a comprehensive overview on atom chips and their applications for cold atoms, ions and molecules.

The Vienna Rb2 setup implements the so-called *side guide trap* [27] geometry to create a single elongated harmonic potential a few tenths of microns below the chip surface. Figure 2.6 sketches the layout of the chip structures used to produce the trapping potential. The following sections describe how the confinement is obtained and discuss the details of the implementation.

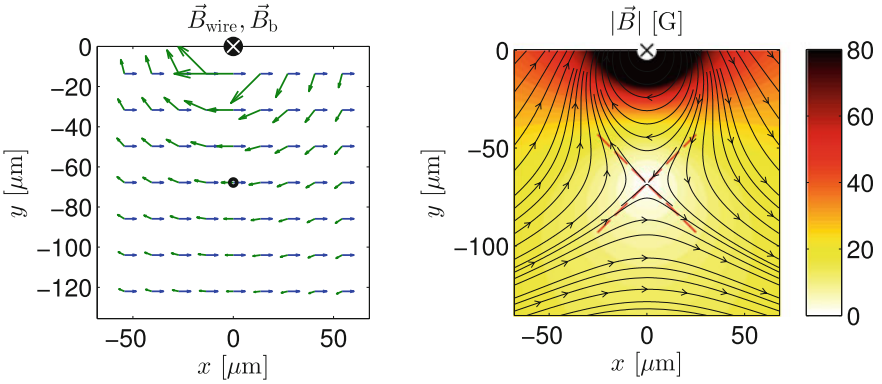

Fig. 2.7 Static transverse confinement. *Left* The uniform bias field (*blue*) and the field created by the trapping wire (*green*) cancel each other in only one point, defining the center of the guide (*black dot*). The direction of the current in the trapping wire is indicated by the cross. *Right* Field magnitude (colorscale) and field lines using the infinite wire approximation. In the vicinity of the point of zero-field, the magnetic field can be approximated by a quadrupole field tilted by 45° with respect to the (x, y) axis (*red lines*) (Color figure online)

Transverse Confinement

An elongated magnetic guide for atoms can be created using a DC current I in a single microwire in combination with a uniform bias field $\vec{B}_{\rm b} = B_{\rm b}\hat{e}_x$ orthogonal to the wire. In the following, we always assume $B_{\rm b} > 0$ and the current I oriented in the same direction as z. In the plane (x, y) orthogonal to the wire, both fields cancel each other in only one point (see Fig. 2.7, left panel). This defines a line of zero-magnetic field parallel to the wire, at a distance

$$d = \frac{\mu_0 I}{2\pi B_{\rm b}} \tag{2.4}$$

(we have assumed a infinitely long and thin trapping wire). For typical parameters $B_b = 29.5$ G and $I = 1$ A, we find $d = 68$ μm. Expanding the field to the first order in the vicinity of the field minimum yields the quadrupole configuration (the origin of the coordinate system is chosen at the point where the magnetic field vanishes)

$$\begin{aligned} B_x &= -Gr\sin\theta = -Gy, \\ B_y &= -Gr\cos\theta = -Gx, \end{aligned} \tag{2.5}$$

with the magnetic gradient at the origin

$$G \equiv \left|\nabla\vec{B}\right| = \frac{B_b}{d} \tag{2.6}$$

(see Fig. 2.7, right panel). This elongated guide does not allow confining atoms efficiently because close to the line of zero-field, they have a high probability to undergo spin flips into non-trapped states [45]. The guide hence has to be plugged by adding a constant offset field B_0 in z direction (Ioffe field). In the vicinity of the potential minimum, the potential reads

$$V_\perp(x, y) = V_0 + \frac{1}{2} m\omega_\perp^2 \left(x^2 + y^2\right) \tag{2.7}$$

with

$$V_0 = \kappa B_0 \tag{2.8}$$

$$\omega_\perp = \sqrt{\frac{\kappa}{m}} \frac{G}{\sqrt{B_0}} = \sqrt{\frac{\kappa}{m}} \frac{2\pi B_\mathrm{b}^2}{\mu_0 I \sqrt{B_0}} \propto \frac{B_\mathrm{b}^2}{I\sqrt{B_0}}. \tag{2.9}$$

For $B_0 = 1.17$ G, the Larmor frequency at the trap bottom[13] $V_0/h \approx 820$ kHz and $\omega_\perp \approx 2\pi \times 3.5$ kHz, satisfying the adiabaticity criterion (2.2). Note that atom chips allow much higher field gradients, and therefore higher trapping frequencies than magnetic trapping geometries using only external coils. In practice, the transverse confinement is varied by changing the Bias field, which also shift the position of the trap.

Longitudinal Confinement

The geometry presented so far creates a cylindrical guide with an isotropic harmonic confinement in the (x, y) plane. To create a confinement in all three directions, the translational invariance along z is broken by a pair of wires (*H-wires*) located at a distance $L/2 = 1$ mm on each side of the main trapping wire (see Fig. 2.6) and orthogonal to the main trapping wire. When a current I_h is sent in each wire (both with the same orientation), a field oriented along z is produced, creating a harmonic potential $V_z(z) = V_\mathrm{TB} + \frac{1}{2} m\omega_z^2 z^2$ with

$$V_\mathrm{TB} = \kappa \left(B_0 + \frac{4d\mu_0 I_h}{\pi L^2}\right), \tag{2.10}$$

$$\omega_z = \sqrt{\frac{\kappa}{m}} \frac{4\mu_0}{\pi L^2} \frac{I_h}{\sqrt{B_0}} \propto \frac{I_h}{\sqrt{B_0}}, \tag{2.11}$$

provided $z, d \ll L$. Since L is much larger than the other length scales, the longitudinal potential is very shallow. The resulting 3D trap is in good approximation an elongated harmonic potential. For a typical current $I_h = 0.5$ A, the correction to the trap bottom due to the H-wires is of the order of 10 % and the expected longitudinal

[13] Simply referred to as: the trap bottom.

frequency is approximately $\omega_z \approx 2\pi \times 15$ Hz, yielding an aspect ratio $\omega_\perp/\omega_z \sim 200$. In practice, however, it is difficult to control the longitudinal frequency close to the chip, as will be explained in the next section.

2.2.1.3 Realistic Static Trap

Finite Size Wires

The model of infinitely long and thin wires presented above gives fair estimates of the trap frequencies and of the trap bottom. In practice, the finite size of the wires cannot be neglected, in particular when d becomes comparable to the width and height of the wires. The dimensions of the wires are given in the caption of Fig. 2.6. In Ref. [9], an analytical expression is given for the field produced by a rectangular wire in three dimensions. We use it to model the chip layout and compute the static field. The parameters of the computation (fields, currents) are calibrated with measured trap parameters (see Sect. 2.2.3). The trap frequencies along the three eigen-axes of the potential are computed by diagonalizing its Hessian matrix at the center of the trap.

The trap frequency is proportional to the field gradient as the position of the trap. As explained in Ref. [46], for a square wire of width and height a, the gradient of the field saturates at a value proportional to I/a. The maximal current applicable is limited by the heat transfer out of the wire, and scales as $a^{3/2}$ [47], so that the maximal gradient scales as $1/\sqrt{a}$, motivating the interest in miniaturized structures.

Gravity

The effect of gravity can also be accounted for in the simulations. It is responsible for a shift of the potential minimum downwards (gravitational sag) of the order of $\Delta y = g/\omega_\perp^2 \sim 30$ nm for typical parameters. For comparison, the half-width of the radial wavefunction is $a_\perp \approx 200$ nm.

Corrugation

An effect which cannot be easily accounted for is the corrugation of the longitudinal potential [8, 46, 48, 49]. Bulk inhomogeneities in the wires, as well as the roughness of the wire surface and edges distort the current flow into directions orthogonal to the wire orientation z. This produces a spatially disordered but temporally constant magnetic field along z, and hence a disordered longitudinal potential $V(z)$. This effect is particularly deleterious close to the chip, where it causes the longitudinal fragmentation of cold atomic clouds when their temperature is of the order of the potential roughness (μK), and sets a limit to the highest achievable aspect ratios of chip traps. For our parameters, corrugation is already dominant in the longitudinal direction, yielding measured trap frequencies significantly higher than the one com-

puted from the finite-size-wire simulations. It seems that the condensate forms in a potential dip created by the corrugation. Still, the additional field in z direction caused by corrugation remains negligible compared to the offset Ioffe field, so that the trap bottom is hardly affected.

It is possible to attenuate the effect of corrugation averaging it out through a rapid modulation of the wire current [50]. This requires however a trapping geometry based on microwires only, since the high inductance of external coils forbids modulation in the kHz range.

2.2.2 *Double-Well Potentials Created by Radio-Frequency Dressing*

The dressing of the internal states of an atom by a strong laser field has been studied extensively and is at the foundation of optical trapping techniques [51]. Using strong rf magnetic fields to couple different internal states of an atom, that experience different spatial potentials, is at the heart of the concept of rf-dressed adiabatic potentials. The spatial dependence of the new energy eigenstates (*dressed states*) emerging from the coupling of the bare atomic states to the rf field can be engineered to create new trapping geometries. A tutorial introduction to rf dressed adiabatic potentials can be found in the Les Houches summer school lecture notes by Perrin [52]

The first rf-dressed adiabatic potentials were proposed in 2001 [53] to realize a 2D curves sheet at the bottom of a magnetic "shell"-potential, and implemented 3 years later [54]. The approach of Ref. [53] was extended by accounting for the vector nature of the magnetic field to propose various trapping geometries including double wells [55], ring traps [55, 56] and periodic arrays of microtraps [57].

The most promiment application of radio-frequency dressing has been the realization of tunable double-well potentials on atom chips. They were used for BEC interferometry [14, 58–61] and to study the dynamics of a superfluid junction [62]. Elongated rf-dressed double wells served as a playground to study pairs of independent [63, 64] or tunnel-coupled [11] 1D quasicondensates. In Refs. [12, 13] and [33], we used rf-dressing to control the anharmonicity of a single elongated potential in order to manipulate coherently motional states of a trapped BEC. Very anisotropic dressed magnetic traps have also been used to study 2D degenerate Bose gases [65].

In Sect. 2.2.2.3, we present the electronics used to radiate the rf fields on the atoms. In Sect. 2.2.2.1, we describe the coupling of a ^{87}Rb atom to an oscillating magnetic field. In Sect. 2.2.2.2, we use the rotating wave approximation (RWA) to derive an approximate expression of the adiabatic potential and show how rf dressing can be used to create a double-well potential. Eventually, we explain how the potential can be computed beyond the RWA (Sect. 2.2.2.4).

2.2.2.1 Coupling of an Atom to an Oscillating Field

Following Lesanovsky et al. [55], we describe the coupling of a ^{87}Rb atom in $F = 1$, $m_F = -1$ to a combination of a static, spatially varying magnetic field, and a uniform oscillating RF field

$$\vec{B} = \vec{B}_s(\vec{r}) + \vec{B}_{RF}\cos(\omega t). \tag{2.12}$$

Since the coupling term (2.1) is local, the Hamiltonian has to be diagonalized for each position in space. For an arbitrary point $\vec{r}$, it is convenient to use a local coordinate system $\{x', y', z'\}$ such that $\vec{B}_s = B_s\widehat{e}_{z'}$ and $\vec{B}_{RF} = B_{RF,\parallel}\widehat{e}_{z'} + B_{RF,\perp}\widehat{e}_{x'}$. In this coordinate system, as a consequence of the adiabaticity hypothesis (2.2), the total angular momentum $\vec{F}$ is also oriented along z'. It means that only the component of the RF field which is orthogonal to z' can couple the different Zeeman states. We introduce the Rabi frequencies for the static and the oscillating field

$$\Omega_s(\vec{r}) = \frac{\kappa}{\hbar}B_s, \tag{2.13}$$

$$\Omega_{RF}(\vec{r}) = \frac{\kappa}{\hbar}B_{RF,\perp}. \tag{2.14}$$

In the basis of the m_F states ($\{-1, 0, 1\}$), the wavefunction obeys the time-dependent Schrödinger equation

$$i\frac{\partial}{\partial t}\begin{pmatrix} c_{-1}(t) \\ c_0(t) \\ c_1(t) \end{pmatrix} = \begin{pmatrix} \Omega_s & \frac{\Omega_{RF}}{\sqrt{2}}\cos(\omega t) & 0 \\ \frac{\Omega_{RF}}{\sqrt{2}}\cos(\omega t) & 0 & \frac{\Omega_{RF}}{\sqrt{2}}\cos(\omega t) \\ 0 & \frac{\Omega_{RF}}{\sqrt{2}}\cos(\omega t) & -\Omega_s \end{pmatrix}\begin{pmatrix} c_{-1}(t) \\ c_0(t) \\ c_1(t) \end{pmatrix}. \tag{2.15}$$

In absence of RF coupling, the stationary solution of (2.15) are the three *bare* m_F states ($\{-1, 0, 1\}$) with the corresponding energies $\{\hbar\Omega_s, 0, -\hbar\Omega_s\}$. The off-diagonal terms mix the bare states into new states **dressed** by the RF field, which are solution of Eq. (2.15).

2.2.2.2 Rotating Wave Approximation

The simplest way to solve Eq. (2.15) consists in making the substitution

$$c_{-1}(t) = \tilde{c}_{-1}(t)e^{-i\omega t}, \tag{2.16}$$

$$c_0(t) = \tilde{c}_0(t), \tag{2.17}$$

$$c_1(t) = \tilde{c}_1(t)e^{i\omega t}, \tag{2.18}$$

which is equivalent to moving to a frame rotating at the frequency of the rf photons. Provided the rf Rabi frequency Ω_{RF} and the detuning $\delta(\vec{r}) \equiv \omega - \Omega_s$ are both small compared to the static Rabi frequency Ω_s, the "rapidly oscillating terms" at $\sim 2\omega$ can be neglected (rotating wave approximation, RWA). This yields the time-independent

Hamiltonian

$$H_{\mathrm{RWA,rot.fr.}} = hbar \cdot \begin{pmatrix} -\delta & \frac{\Omega_{\mathrm{RF}}}{2\sqrt{2}} & 0 \\ \frac{\Omega_{\mathrm{RF}}}{2\sqrt{2}} & 0 & \frac{\Omega_{\mathrm{RF}}}{2\sqrt{2}} \\ 0 & \frac{\Omega_{\mathrm{RF}}}{2\sqrt{2}} & \delta \end{pmatrix}. \tag{2.19}$$

The new "dressed" energy levels

$$V\left(\vec{r}\right) = m'_{\mathrm{F}}\hbar\sqrt{\delta^2\left(\vec{r}\right) + \frac{1}{4}\Omega^2_{\mathrm{RF}}\left(\vec{r}\right)}. \tag{2.20}$$

arising from the coupling of the atom to the magnetic field are found by diagonalizing the RWA Hamiltonian. Their are labeled by the new quantum number $m'_{\mathrm{F}} \in \{-1, 0, 1\}$. Inserting the approximate expression for the static field

$$\vec{B}_{\mathrm{s}}\left(\vec{r}\right) = -Gr\left(\sin\theta\hat{e}_x + \cos\theta\hat{e}_y\right) + B_0\hat{e}_z, \tag{2.21}$$

the RWA potential reads, in polar coordinates [55]:

$$V_{\mathrm{RWA}}\left(r,\theta\right) = m'_{\mathrm{F}}\kappa\sqrt{\left(B_{\mathrm{s}} - \frac{\hbar\omega}{\kappa}\right)^2 + \left(\frac{B_{\mathrm{RF}}}{2\left|B_{\mathrm{s}}\right|}\right)^2\left[B_0^2 + G^2r^2\left(\cos\alpha\sin\theta + \sin\alpha\cos\theta\right)^2\right]}, \tag{2.22}$$

where α is the angle between the direction of the rf magnetic field and the vertical axis:

$$\vec{B}_{\mathrm{RF}} = B_{\mathrm{RF}}\left(-\sin\alpha\hat{e}_x + \cos\alpha\hat{e}_y\right). \tag{2.23}$$

(see Fig. 2.8).

The static potential is approximately harmonic and transversely isotropic. If the rf amplitude is increased (keeping the rf frequency constant), the potential smoothly becomes anisotropic and flattens along a direction tilted by $-\alpha$ with respect to the x-axis. In Refs. [12, 13, 33], we took advantage of the anisotropy and anharmonicity induced by weak rf dressing to single out the two lowest vibrational levels and manipulate non-classical motional states of a trapped BEC. The axis of splitting (red line in Fig. 2.8) corresponds to the direction where the quadruopole component of the static magnetic field is parallel to the rf field [59].

Above a certain critical value B_{c} of the rf dressing amplitude, a potential hump emerges at the center of the trap, creating two minima along the splitting axis. If the rf intensity is further increased, the distance between the minima gets larger while the potential barrier rises. This geometry hence allow to create a tunable double well controlled by the amplitude[14] of the rf field. In Ref. [55], Lesanowsky et al. give

[14] It is also possible to split the potential by ramping the rf frequency towards the Larmor frequency of the static trap, as was done for example originally in Ref. [58].

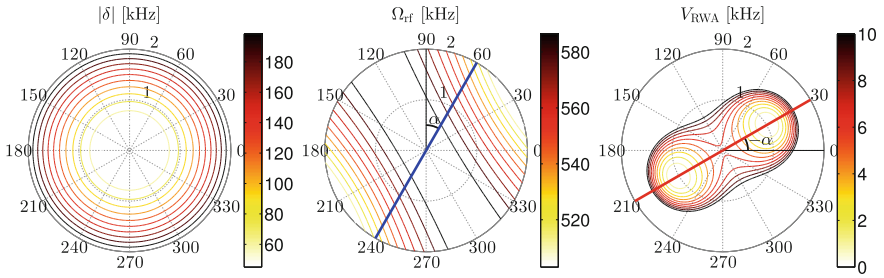

Fig. 2.8 Dressed double-well potential within the RWA. All energies are given in kHz, polar representation in the transverse (x, y) plane (polar radius in μm, polar angle in °). *Left* Detuning term. For a negative detuning ($\omega < \Omega_s$), it simply corresponds to the transversely isotropic parabola of the static potential. *Center* RF Rabi frequency. *Blue line* direction of polarization of the RF field ($\alpha = -30°$). The coupling to the RF breaks the polar symmetry by creating a potential barrier oriented along $-\alpha$ with respect to the y axis. *Right* The resulting RWA potential (Eq. (2.22)) exhibits two local minima along an axis (*red line*) tilted by an angle $-\alpha$ with respect to the x axis. The origin of energies is chosen at the minima of the potential. Same parameters as in Sect. 2.2.1.2 and $\delta = -2\pi \times 30$ kHz and $B_{RF} = 0.85$ G (Color figure online)

useful approximate expressions for the position $\pm r_0$ of the potential minima, the angular trap frequency ω_{dw} of each well along the splitting axis, the correction to the trap bottom B_{TB} and the critical splitting field B_c:

$$r_0 = \frac{1}{\sqrt{2}G}\sqrt{B_{RF}^2 - B_c^2}, \tag{2.24}$$

$$\omega_{dw} = \sqrt{\frac{\kappa}{mB_{TB}}}\frac{G^2 r_0}{B_0}, \tag{2.25}$$

$$B_{TB} = \frac{B_{RF}}{2}\sqrt{1 - \frac{\hbar\delta_0}{\kappa B_0}}, \tag{2.26}$$

$$B_c = 2\sqrt{-B_0\frac{\hbar\delta_0}{\kappa}} \tag{2.27}$$

($\delta_0 \equiv \omega - \kappa/\hbar B_0$ is the detuning at the minimum of the static trap. For our parameters, $\delta_0 < 0$). Equations (2.24)–(2.27) do not always give accurate quantitative predictions, but they capture the right dependence on the rf amplitude B_{RF} and the detuning δ_0.

Conveniently, the transverse double-well potential can generally be well approximated by the simple polynomial [59]

$$V_{DW} = bx^2 + dx^4. \tag{2.28}$$

It is important to keep in mind that when tuning the double well with one control parameter only (in our case the rf dressing amplitude), r_0 and ω_{dw} cannot be adjusted independently. We will see in Sects. 3.4.1 and 3.6.1 that this sets some constraints on ensuring adiabatic motion of the condensate in the double well.

It is also interesting to note that Eq. (2.22) allows also to realize a double well with positive detuning ($\hbar\omega > \kappa B_0$). The main difference is that the spatial dependence of the detuning term has the shape of the bottom of a bottle-of-wine, with a "resonant ring" of points where the detuning term vanishes ($\Omega_s(\vec{r}) = \omega$). This causes a larger well spacing than in the negative detuning case, for the same rf amplitude (see Eq. (2.24)), but also a higher sensitivity of the well position to noise on the Ioffe field. For a full analysis of the effects of noise on the double well, see the Ph.D. thesis of Schumm [8].

2.2.2.3 Implementation

The rf magnetic field is induced by AC currents sent through two wires (width: 10 μm) parallel to the main trapping wire, located on each side at a distance of $l = 55\,\mu\text{m}$ (see Fig. 2.6, right panel). Peak-to-peak intensities up to ∼100 mA can be sent through each wire, resulting in rf field amplitudes up to ∼2.5 G. In first approximation, the rf field can be considered uniform over the region where the atoms are trapped. Its polarization can be tuned by varying the relative intensity between both wires as well as their relative phase

$$\begin{aligned} I_{\text{RF1}} &= I_1 \left(\cos \omega t\right), \\ I_{\text{RF2}} &= I_2 \left(\cos \omega t + \phi_{12}\right), \end{aligned} \tag{2.29}$$

where ω is the angular frequency of the RF (by convention, the amplitudes $I_1, I_2 \geq 0$). To create double-well potentials with an arbitrary splitting axis in the (x, y) plane, the rf field must be linearly polarized, meaning that $\phi_{12} = 0$ or π. To rotate the double well in the (x, y) plane by an angle $-\alpha$ with respect to the horizontlal (x)-axis (see Fig. 2.8), $\vec{B}_{\text{RF}}$ must be rotated by an angle $+\alpha$ with respect to the vertical (y)-axis (see Fig. 2.6, right panel). To keep the well spacing constant when changing α, the amplitudes I_1, I_2 and the relative phase ϕ_{12} must obey

$$\begin{aligned} I_1 &= I_0 \left|\cos\alpha - \frac{\sin\alpha}{\tan\beta}\right|, \\ I_1 &= I_0 \left|\cos\alpha + \frac{\sin\alpha}{\tan\beta}\right|, \\ \phi_{12} &= 0 \text{ if } \alpha \bmod [\pi] \in [\beta, \beta + \pi/2], \ \phi_{12} = \pi \text{ otherwise.} \end{aligned} \tag{2.30}$$

Here $\tan\beta = d/l = 42.5°$ and I_0 is the amplitude in each wire for a vertical polarization ($\alpha = 0$), as required for a horizontal double well: $I_1 = I_2 = I_0, \phi = \pi$. Note that the polarization axis can be rotated on $[0, 2\pi]$ without discontinuity of the current because each time ϕ_{12} jumps between 0 and π, either I_1 or I_2 is equal to 0.

To achieve full control over amplitudes and phase, each rf wire is connected to a separate output of the digital arbitrary waveform generator. Although it can be programmed to generate arbitrary signals, we used it only to produce sinusoidal

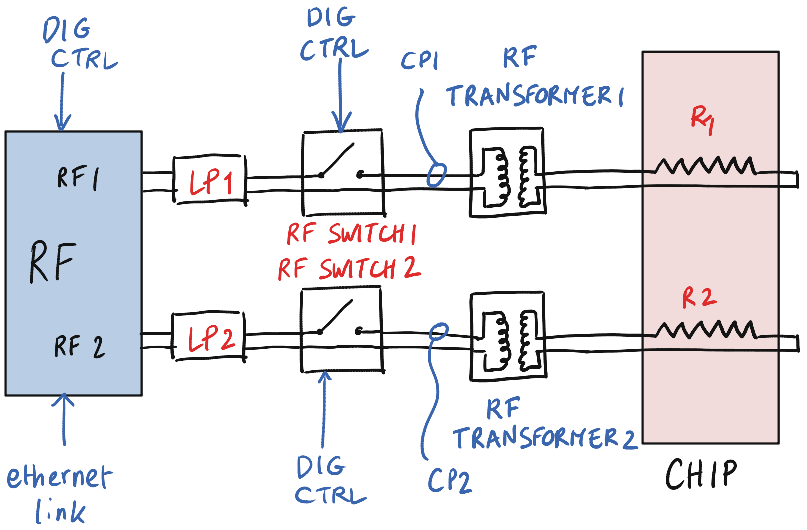

Fig. 2.9 Schematics of the rf electronics. The two rf microwires, with resistance $R_{1,2} \approx 44\,\Omega$ are connected each to one output of the digital arbitrary waveform generator through a low-pass filter ($LP_{1,2}$), a rf switch (MiniCircuits ZX80-DR230-S+) and a 1:1 rf isolation transformer (MiniCircuits T1-1T) to ensure a floating ground. The rf source is controlled digitally through an Ethernet link and can be triggered with a TTL signal. Both channels ($RF_{1,2}$) can be controlled independently. Two low pass filters (cutoff frequency: 1.9 MHz) are used to suppress higher harmonics of the DDS generator. The rf switches can also be triggered, bust most of the time the switching on and off was performed using the rf output. Two alternative current probes (Tektronix CT-6, $CP_{1,2}$) were used to monitor the rf currents on an oscilloscope. Note that although the two rf circuits are in principle identical, they may have different response functions, so that the current balance and the relative phase have to be adjusted carefully on a common probe

signals with time-dependent amplitudes. Figure 2.9 shows a schematics of the RF control electronics. The main limitation to the complexity of the rf control sequence is set by the capacity of the memory of the digital RF source. Although basic patterns, such as a period of a sine wave at constant amplitude, can be indefinitely looped, the rf amplitude *ramps* had to be programmed point by point. To allow decreasing the sampling rate of the arbitrary waveform generator without distorting the signal, low-pass filters (cutoff frequency: 1.9 MHz) were added at the output of each rf channel. The maximum ramp duration for our rf dressing carrier frequency of 880 kHz allowed a maximum total ramp duration (for each channel) of more than 55 ms, limited by the size of the memory. An analog control of the amplitude of the RF source is also available, but it doesn't allow tuning each output independently, as needed to turn the polarization of the RF field, and it is expected to be noisier than the sole digital control.

For the experiments presented in the next chapters, RF currents up to $I_0^{\max} = 79.5$ mA pp (in the case of horizontal splitting, $\alpha = 0$) were used. In the rest of this thesis, instead of giving the absolute value of the current in mA pp, we will often refer

to the RF amplitude $\mathrm{RF}_{\mathrm{Amp}}$ in units of $I_0^{\max}$ ($0 \leq \mathrm{RF}_{\mathrm{amp}} \leq 1$). The corresponding values of $I_{1,2}$ and ϕ_{12} for a tilted RF polarization are given by Eq. (2.30).

2.2.2.4 Beyond the Rotating Wave Approximation

For the dressed potential presented in this thesis, $|\delta| = 30$ kHz $\ll \Omega_{\mathrm{s}} = 910$ kHz at the center of the trap. Nevertheless, high rf amplitudes, up to $\Omega_{\mathrm{RF}} \gtrsim \Omega_{\mathrm{s}}$ are commonly used to achieve large splitting distances ($2r_0 \sim 4$ μm). It is therefore necessary to compute the dressed potential beyond the RWA. The standard method to solve a Schrödinger equation with any periodic, time-dependent Hamiltonian has been given by Shirley in 1965 [66]. In our case, it consists in transforming the system of three differential equations (2.15) into an infinite system of linear equations with time-independent coefficients. This is achieved by expanding the time-dependent coefficients of the wavefunction as Fourier series

$$c_{-1}(t) = \sum_{n\in\mathbb{Z}} c_{-1}^{(n)} e^{-i(n+1)\omega t}, \tag{2.31}$$

$$c_0(t) = \sum_{n\in\mathbb{Z}} c_0^{(n)} e^{-in\omega t}, \tag{2.32}$$

$$c_1(t) = \sum_{n\in\mathbb{Z}} c_1^{(n)} e^{-i(n-1)\omega t}. \tag{2.33}$$

Solving Eq. (2.15) (for each point of space) is then exactly equivalent to diagonalizing the infinite-dimension matrix

$$M = \begin{pmatrix}
\ddots & & & & & & & & & & & & & \\
0 & 0 & 0 & a+\omega & b & 0 & 0 & 0 & 0 & b & 0 & 0 & 0 & 0 \\
0 & 0 & 0 & b & 0 & b & 0 & 0 & 0 & 0 & b & 0 & 0 & 0 \\
0 & 0 & 0 & 0 & b & -a+\omega & 0 & 0 & 0 & 0 & 0 & 0 & 0 & 0 \\
0 & 0 & 0 & 0 & 0 & 0 & a & b & 0 & 0 & 0 & 0 & b & 0 \\
b & 0 & 0 & 0 & 0 & 0 & b & 0 & b & 0 & 0 & 0 & 0 & b \\
0 & b & 0 & 0 & 0 & 0 & 0 & b & -a & 0 & 0 & 0 & 0 & 0 \\
0 & 0 & 0 & 0 & 0 & 0 & 0 & 0 & 0 & a-\omega & b & 0 & 0 & 0 \\
0 & 0 & 0 & b & 0 & 0 & 0 & 0 & 0 & b & 0 & b & 0 & 0 \\
0 & 0 & 0 & 0 & b & 0 & 0 & 0 & 0 & 0 & b & -a-\omega & 0 & 0 \\
 & & & & & & & & & & & & & \ddots
\end{pmatrix}, \tag{2.34}$$

with

$$a \equiv \Omega_{\mathrm{s}}, \tag{2.35}$$

$$b \equiv \frac{\Omega_{\mathrm{RF}}}{2\sqrt{2}}. \tag{2.36}$$

M consists of 3×3 diagonal blocks (for example, red block in the center) and off-diagonal terms (blue). M has an infinite number of eigenvalues which, due to the invariance by the transformation $\omega \rightarrow p + \omega$ (for any integer p) are all equal to one of three principal eigenvalues, modulo ω. In practice, it can be diagonalized approximately by truncating M to a finite sized matrix and keeping the three central eigenvalues.

The physical meaning of these blocks becomes obvious when writing the magnetic field in the formalism of second quantization (see for example Ref. [67]). They are associated to processes implying the exchange of more than one rf photon. Diagonalizing the full quantum-mechanical Hamiltonian shows that the dressed states are grouped into three-state manifolds separated by one rf photon energy (see Fig. 2.10, taken from Perrin's lecture notes [67]). The summation over $\mathbb{Z}$ in the Fourier series expansion implicitly means that the field is assumed to contain an infinite (very large) number of photons, as it is the case with a classical coherent field. Retaining only one Floquet multiplicity (red central block in (2.34)) is equivalent to applying the RWA, see Eq. (2.19) for comparison. It implies neglecting the non-resonant coupling terms

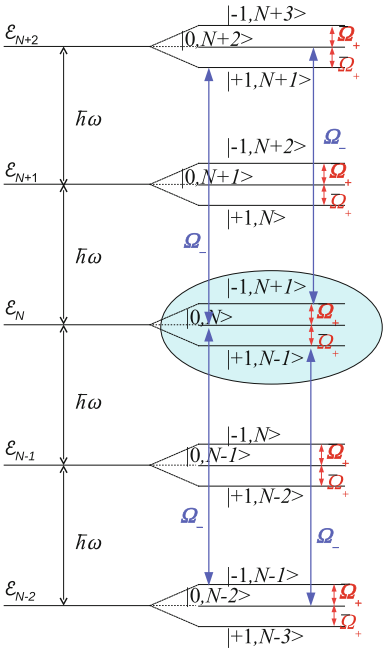

Fig. 2.10 Schematics of the dressed states picture. Taken from Perrin's lecture notes [67]. The dressed states of the atom and the electromagnetic field can be groupped into three-state manifolds separated by one photon energy $\hbar\omega$. In the RWA, only the coupling terms within one manifold are retained (*red arrows* and *red* terms in Eq. 2.34), and each manifold can be treated independently (*blue bubble*). The *blue* terms (*blue arrows*) couple the nth manifold to $n + 2$ and $n - 2$ and are responsible for beyond RWA effects, which cannot be neglected when Ω_{RF} or Δ become comparable to Ω_s and the manifolds are not clearly decoupled (Color figure online)

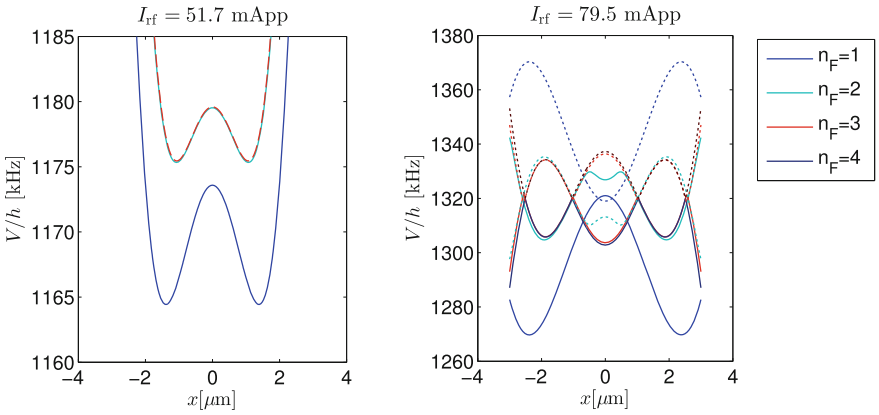

Fig. 2.11 Beyond RWA calculation of the dressed potential. *Left* Potential computed retaining $n_F = 1, 2, 3$ Floquet multiplicities at a moderate rf intensity. Taking into account the first order correction to the RWA ($n_F = 2$) differs significantly from the RWA result ($n_F = 1$). However, increasing n_F above 2 doesn't improve much the result. *Right* (For each n_F, both $m'_F = \pm 1$ are represented by a *full* and *dashed line* respectively). For even higher rf intensities, needed for the full separation of the clouds, the coupling between the multiplicities leads to avoided crossings which complicate the calculation of the potential experienced by the atoms. Whether or not the atoms see the avoided crossing depends on their velocity (see Sect. 2.2.1.1)

to the $n+2$ and $n-2$ multiplicities (blue terms in (2.34) and blue arrows in Fig. 2.10). This is valid as long as the detuning is small enough so that the multplicities do not overlap, and as long as the rf Rabi frequency is weak enough to neglect the coupling between different multiplicities. In practice, for our parameters, it is enough to retain up to $n_F = 5$ Floquet multiplicities for the numerical computations (see Fig. 2.11).

2.2.3 *Characterization of the Potential and Calibration of the Simulations*

The quantitative description of the dynamics of the condensate in the double well requires a precise knowledge of the shape of the potential. This is achieved by computing it as explained in the previous section. The parameters of the simulations are adjusted using measurements of the trap. This section describes the whole calibration procedure which has been used to simulate the traps in which the experiments of Chap. 3 have been performed. The good agreement between measurement and simulations of many different quantities is a convincing demonstration of the reliability of the calibration procedure. This section is organized as follows: first, the calibration of the static trap is presented, then that of the rf dressing and of the dressed potentials.

2.2.3.1 Static Trap

To calibrate the static trap, we use the fact that the trap bottom V_{TB} depends essentially on the Ioffe field B_0 and the current in the longitudinal confinement wires I_{h} (see Eq. 2.10), while the radial trap frequency depends mainly on the bias field B_{s} and the current I in the main trapping wire (with a weak dependence on the Ioffe field, see Eq. 2.9). The trap bottom is measured by means of rf spectroscopy, while the trap frequencies along the three eigenaxes of the potential are measured by exciting dipolar oscillations of a condensate (see Fig. 2.12).

Trap Bottom Spectroscopy

The value of the Larmor frequency at the center of the trap $\nu_{\mathrm{TB}} = V_{\mathrm{TB}}/h$ is probed by means of rf spectroscopy [68]. We use the same rf electronics as for the evaporative cooling, but strongly reduce the rf intensity to resonantly couple atoms between the trapped state $m_{\mathrm{F}} = -1$ and the untrapped state $m_{\mathrm{F}} = 0$ without dressing the potential. We apply a $T = 20$ ms pulse rf pulse at constant frequency ν_{RF} onto the trapped condensate. At resonance, i.e. when $\nu_{\mathrm{RF}} = \nu_L$, atoms are maximally coupled

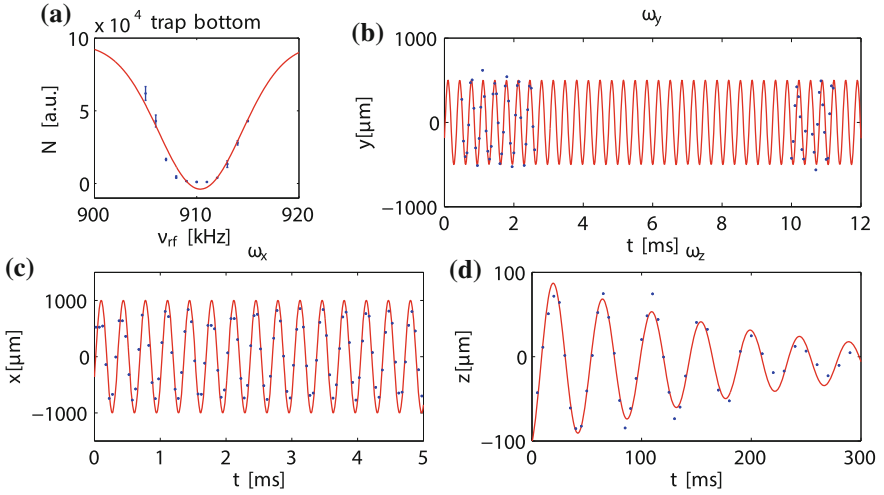

Fig. 2.12 Static trap characterization. **a** Trap bottom spectroscopy. A weak rf pulse is applied to resonantly outcouple atoms from the trap. The maximum losses (dip) is achieved when the rf frequency is equal to the Larmor frequency in the center of the trap. The *red line* is a guide to the eye. **b–d** Trap frequencies in transverse horizontal (**b**), transverse vertical (**c**) and longitudinal (**d**) direction, obtained by exciting dipolar oscillations (sloshing) and measuring the position of the center-of-mass after expansion. Note the difference of time scale between transverse and longitudinal oscillations, as well as the damping of the longitudinal sloshing. It is probably due to the anharmonicity of the longitudinal potential caused by corrugation, as well as technical heating. The values of the trap parameters are summarized in Table 2.1 (Color figure online)

to $m_F = 0$ and fall off the trap. After a few ms of holding time ensuring that the outcoupled atoms leave the imaging region, the remaining atoms are released and counted. The trap bottom is inferred from the frequency of the loss dip in the number of remaining atoms when ν_{RF} is scanned (see Fig. 2.12a).

The width of the loss dip is influenced by several effects, including: power broadening (the intensity of the rf spectroscopy pulse has to be chosen weak enough), the resolution in frequency (the pulse duration $T = 20$ ms imposing $\Delta\nu = 1/T = 0.05$ kHz was chosen in order to average over one period of the characteristic 50 Hz electric noise), the stability of the trap bottom (dominated by the stability of the Ioffe field B_0, see [1]), the chemical potential of the condensate ($\mu/h \sim 1$ kHz) and the gravitational sag [69]. For most experiments, the typical rms width of the static trap spectroscopy was about 4 kHz.

Note that the same technique can be used in rf dressed trap to measure the effective trap bottom by coupling atoms between the trapped dressed state and $m'_F = 0$. In Ref. [70], this technique has been used to demonstrate the existence of beyond RWA resonances between different Floquet multiplicities. We observe that resonances in the dressed potentials are typically twice narrower than in the static trap (see Fig. 2.14, upper panel). This might come from the fact that the effective trap bottom is twice less sensitive to fluctuations of B_0 (see Eq. (2.26)), because a variation of B_0 is partly compensated by a variation of the detuning, similarly to what has been investigated in Ref. [71].

Trap Frequencies

The trap frequencies are probed by exciting dipolar (sloshing) oscillations of the condensante along each of the three eigenaxis of the nearly harmonic potential.

In the **vertical transverse direction** (y), a small kick is applied by suddenly ($< 25\,\mu$s) varying the current in the main trapping wire by $\sim$1 %. It excites a center-of-mass oscillation of amplitude approximately four times the transverse oscillator length. The motion is recorded by imaging the atoms in the (z,y) plane with the absorption imaging system (see Sect. 2.3.1) after 17 ms tof (see Fig. 2.12b).

In the **horizontal transverse direction** (x), the condensate is prepared in one well of a horizontal (dressed) double-well potential (this is achieved by slowly splitting the condensate in the vertical direction, and then leveling the double well). The rf current is then rapidly ramped off so that the position of the cloud does not change. The atoms find themselves displaced horizontally with respect to the center of the static trap and start oscillating (see Sect. 3.2.2.1. The motion is recorded by imaging the atoms with the "light sheet" imaging system Sect. 2.3.2 in the (x, y) horizontal plane after 46 ms of tof (see Fig. 2.12c).

The **longitudinal frequency** ω_z is measured by slowly, slightly distorting the longitudinal potential, and returning abruptly to the original potential. This is achieved by means of a weak current pulse produced by a wire (see Fig. 2.6) orthogonal to the main trapping wire. The measurement of the slow longitudinal sloshing (typical frequency: 20 Hz) is limited by its damping time (typically 200 ms, see Fig. 2.12d),

Table 2.1 Trap calibration

Measured parameters	
Trap bottom V_{TB}/h	910 ± 1 kHz
Horizontal transverse trap freq. $\omega_x/2\pi$	2.97 ± 0.01 kHz
Vertical transverse trap freq. $\omega_y/2\pi$	2.98 ± 0.01 kHz
Longitudinal trap freq. $\omega_z/2\pi$	22.3 ± 0.3 Hz
Settings used for simulations	
Current in main trapping wire I	1 A
Current in longitudinal confinement wires I_{h}	0.5 A
Bias field B_{b}	29.5 G
Ioffe field B_0	1.17 G
Max. rf current (in each wire) $I_0^{\max}$	79.5 mApp
rf relative phase ϕ_{12}	$-2°$

Upper part measured trap parameters, with the corresponding experimental uncertainty. *Lower part* Parameters used in the chip trap simulations

associated to the heating of the cloud and the anharmonicity caused by potential corrugation.

Calibration of the Static Trap Simulations

The currents in the main trapping wire and in the longitudinal confinement wire I and I_{h} are measured with a precision multimeter meter[15] and the values are used for computation of the potential. The value of B_0 for the simulation is adjusted to match approximately the measured trap bottom. Both values of B_0 and B_{b} are iteratively fine-tuned to reproduce exactly the measured radial trap frequencies and trap bottom. This leaves some indeterminacy between B_0 and B_{b}, which can then be lifted from the measurements of the dressed trap (see next section). The potential simulations usually strongly underestimate the longitudinal trap frequency (typically by a factor 4) because they do not take corrugation into account. Table 2.1 summarizes the values of the measured trap parameters and the corresponding settings for the simulations.

2.2.3.2 RF Dressing

Once the static trap has been characterized, the rf dressing must be calibrated. The first step is to characterize and adjust the rf amplitudes I_1 and I_2 in each wire as well as the relative phase ϕ_{12} (see Eq. (2.29)). The second step is to adjust and check these parameters in the simulation by comparing them to measurements of

[15] Keithley 2000 digital Multimeter.

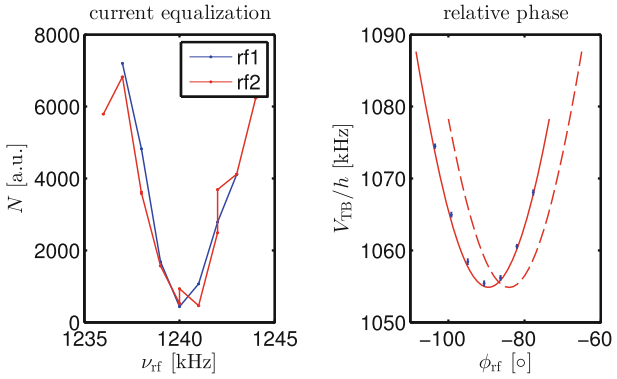

Fig. 2.13 Adjustment of the RF intensity balance and the relative phase. *Left* The trap bottom spectroscopies for a trap dressed by only RF wire at a time overlap, ensuring that $I_1 = I_2$. *Right* The effective trap bottom is measured as a funtion of the relative phase ϕ_{12} between the two wires (*blue dots*). The result of the simulations has to be shifted by approximately 6° to match the measurement. This is probably caused by some differential filtering in the RF electronics of each channel (Color figure online)

the effective trap bottom, trap frequencies, well spacing etc. in a series of dressed potentials obtained for different rf intensities.

Balance of the RF Currents in the Two Wires

The rf generator produces a given AC voltage. Since the resistance of each wire (including the leads and the rf electronics for each output port) may be different, the currents have to be balanced using a common probe. The high-frequency current probes mounted on each wire give an estimate of the currents, but the atoms are a much more precise probe of the magnetic field. For some arbitrary intensity I_0, the effective trap bottom is measured by rf spectroscopy with one rf wire on at a time. The voltage of each output port of the rf source is tuned to equalize the trap bottoms (see Fig. 2.13, left panel), ensuring $I_1 = I_2$. Furthermore, comparing the measured value of the trap bottom to simulations enables to calibrate the absolute values of $I_{1,2}$.

Relative Phase Between the RF Wires

The control of the relative phase between the two rf wires is important to ensure the right linear polarization to turn the axis of the double well. Different delays due to different filtering in the rf leads may shift ϕ_{12} with respect to the value defined by the rf generator. This effect is accounted for by correcting the phase difference between the two output of the rf generator by an amount which is determined by

measuring the dependence of the trap bottom with respect to the relative phase (see Fig. 2.13, right panel). The dependence of the effective trap bottom with ϕ_{12} is not trivial but can be simulated. It is related to the relative contribution of the σ^+ and σ^- polarization which couple the different m_F states. Note that the geometry of the dressed potential can change between a double well and a ring trap, depending on ϕ_{12} [55]. We found that ϕ_{12} had to be corrected by 6° with respect to the nominal value to get a linear polarization. For the experiments presented in chapter , this value has been slightly over-corrected. For this reasons, all simulations of the potential were performed with $\phi_{12} = -2°$.

Additional Checks

In principle, the calibration procedure presented above is sufficient to constraint all parameters of the static trap and of the rf dressing. Nevertheless, a series of additional measurements were performed to benchmark the simulations of the potential.

The dependence of the effective trap bottom with the rf amplitude was checked, recovering the linear behaviour given by Eq. (2.26) (see Fig. 2.14).

The transverse trap frequencies in each well of the dressed potentials were also compared to simulations (see Fig. 2.15, left pannel). The vertical trap frequency was measured in the same way as in Sect. 2.2.3.1. The horizontal trap frequency ω_{dw} (Eq. (2.25)) was measured by slightly changing the rf amplitude to excite an oscillation of the spacing between the two parts of the condensate in the double-well. This results in an oscillation of the fringe spacing of the interference pattern measured after tof (see Sect. 3.2.1). Note that in this strongly anharmonic direction, the notion of trap frequency is less obvious, explaining partly the poor agreement of experiment and simulation.

The spacing $d = 2r_0$ between the two wells (Eq. (2.24)) was also inferred from the fringe spacing of the interference patterns. Assuming Gaussian wave packets and a ballistic expansion during a time t, the fringe spacing is

$$\lambda \approx \frac{ht}{dm}. \tag{2.37}$$

It shows a very good agreement with the simulations for strongly split double wells, where the effect of interactions is less significant [58].

Note that for both d and ω_{dw}, the beyond-RWA simulations are in excellent agreement with the dependence on the rf dressing amplitude expected from the approximate RWA expressions (2.24) and (2.25). Fitting them to the data of Fig. 2.15, we found that the critical splitting point is reached for $\mathrm{RF}^{c}_{\mathrm{Amp}} = 0.42$.

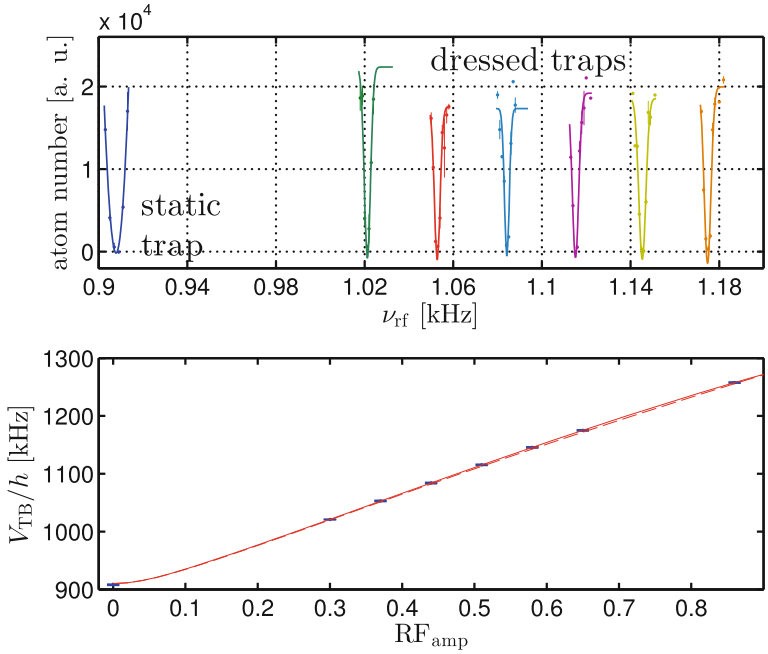

Fig. 2.14 RF amplitude calibration. The effective trap bottom $V_{\rm TB}$ is measured by rf spectroscopy for different values of the amplitude of the rf current ($I_1 = I_2$). *Top panel* rf spectroscopies for 5 values of $RF_{\rm Amp}$ between 0 and 0.65 (five first points of *bottom panel*). Note that the loss dips are narrower in the dressed potentials as compared to the static trap. *Bottom panel* effective trap bottom $V_{\rm TB}/h$ as a function of $RF_{\rm Amp}$, showing good agreement with the beyond RWA simulations. Note that the RWA prediction (*dashed curve*) underestimates the trap bottom by a few kHz only

2.3 Imaging Systems

Most of the experimental information gathered on Bose-Einstein condensates in atomic gases has been obtained by optical measurements, that is to say photographs of the atoms. Notable exceptions are for example the temporally and spatially resolved detection of a BEC of metastable Helium with a microchannel plate [72] or the use of scanning electron microscopy (SEM) [73].

Among the various optical imaging methods used to probe ultracold gases [74], two independent systems are implemented on the Rb2 setup (see Fig. 2.16):

- an absorption imaging system,
- and a fluorescence imaging (often referred to as *Light Sheet*).

Both allow imaging destructively the atom cloud in tof, meaning that for each experimental cycle, the atomic sample can be observed only once. Figure 2.17 shows typical images of condensates taken with both imaging systems. The following section briefly presents both imaging systems, with emphasis on the methods we

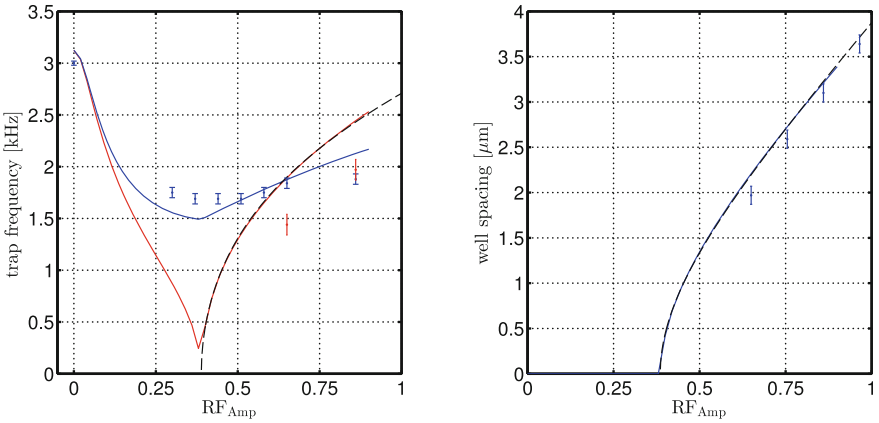

Fig. 2.15 Transverse trap frequencies and well spacing. *Left* Transverse trap frequencies (quadratic term in the Taylor expansion of the potential) in the double-well (*red* ω_{dw} in the direction of splitting, *blue* orthogonal direction) as a function of the rf amplitude. *Points* measurements. *Lines* beyond RWA simulations. *Black dashed* fit of the beyond RWA simulation with the approximate expression (2.25). Note the typical kink of ω_{dw} at the critical value $\mathrm{RF}^{\mathrm{c}}_{\mathrm{Amp}} = 0.42$, corresponding to the splitting point. *Right* Spacing between the potential wells, inferred from (3.2). *Points* measurement. *Blue line* beyond RWA simulation. *Black dashed line* fit of the beyond RWA simulation with the approximate expression (2.24). Note that both quantities are very well described qualitatively by the RWA approximate analytical expressions (Color figure online)

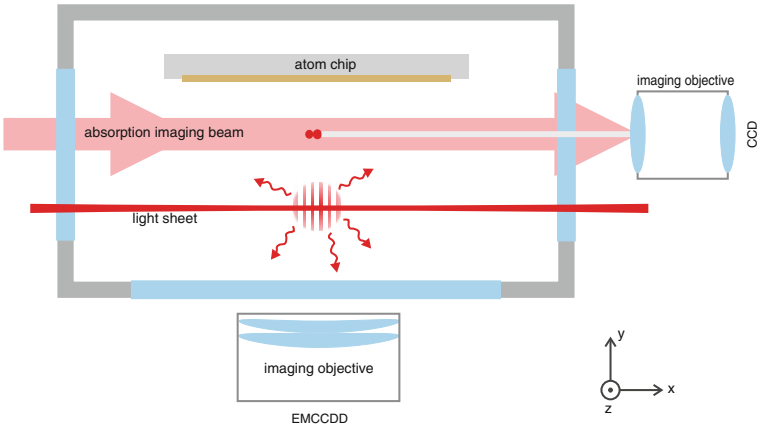

Fig. 2.16 Schematics of the two imaging systems. The absorption beam is oriented along the x-axis to image the atoms in a plane parallel to the long axis of the trap (z). The shadow cast by the atoms is imaged through an objective on a CCD camera. The fluorescence imaging is oriented along the y-axis to image photons scattered by the atoms while falling through the light sheet. Light is collected by an objective located below the chamber and detected by a EMCCD camera. When the BEC is released from a horizontal double well, imaging along (x) integrates over the matter-wave interference pattern, while the fringes can be resolved with the fluorescence imaging system

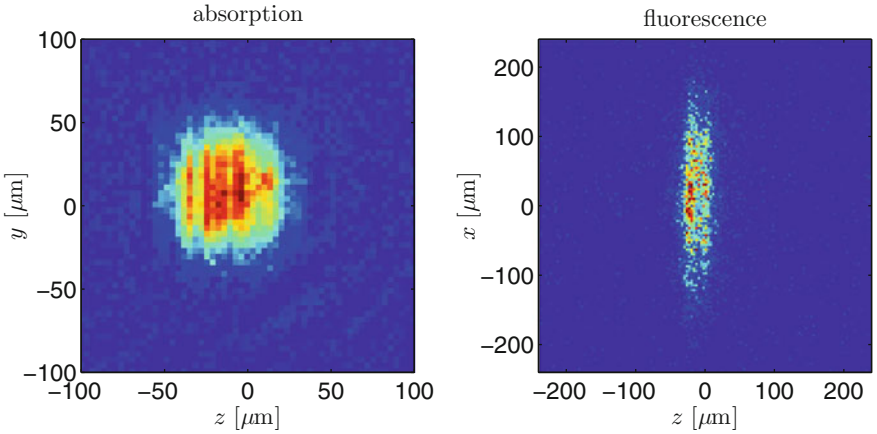

Fig. 2.17 Images of quasi-condensates. Pictures of quasi-BECs with ∼1000 atoms taken 6 ms (absorption imaging system, *left*) and 46 ms (fluorescence imaging systems, *right*) after release from a (in this case single-well) trap. The axes are the same as in Fig. 2.16: (z) is the axis of shallow confinement and gravity is oriented along (y). Note that both pictures exhibit characteristic patterns perpendicular to the (z)-axis. They correspond to density fluctuations emerging in tof as a result of the initial longitudinal phase fluctuations [16]

used to determine the absolute atom number in our condensates. A more detailed description of the hardware as well as the characterization of both imaging systems can be found in the diploma and Ph.D. thesis of Bücker [1, 18] as well as in the Ph.D. theses of Manz [16] and Betz [10].

2.3.1 Absorption Imaging

Absorption imaging is probably the most commonly used imaging technique in cold atom experiments [74]. A comprehensive discussion of absorption imaging on atom chip setups can be found in Ref. [75]. The Ph.D. theses of Gring [76] and Jacqmin [77] contain detailed descriptions of absorption imaging systems implemented in different configurations on atom chip experiments similar to our setup.

The absorption imaging system implemented on Rb2 is oriented along the x-axis to image the atoms in the (y, z) plane. It allows inferring the integrated column density $\tilde{n}(y, z) = \int n(\vec{r})dx$ from the attenuation of a laser beam passing through the atomic cloud [74]. The shadow cast by the atoms is imaged onto a back illuminated Charge Coupled Device camera[16] (CCD) through an objective consisting of two doublet lenses, each operating at near-infinite conjugate ratio. The optics is adjusted to obtain a magnification of $\times 3.78$. The corresponding pixel size (in object space) is $3.44 \times 3.44\ \mu\text{m}^2$. The numerical aperture (NA) of 0.12 determines the diffraction

[16] Princeton Instruments MicroMax 1024 BFT.

limit, which lies slightly below 4 μm. The field of view (3 × 3 mm) allows for tofs up to ∼25 ms. When the cloud is imaged too close to the chip (tof $\lesssim$ 2 ms), unavoidable reflection and refraction of the imaging light on the surface of the chip cause distortions of the image [75]. The fast frame-transfer readout enables taking the absorption and the reference picture within tens of ms, in order to mitigate the effect of mechanical vibrations.

The absorption imaging system can be used to image thermal clouds (after short tofs) or BECs. We use it routinely to monitor center-of-mass oscillations in order to measure trap frequencies (see Sect. 2.2.3.1), image BECs after short tofs (2 ms) to access their *in-situ* density profile, and to measure the atom number in our BECs (see next section). In Ref. [20], it was used to measure density fluctuations (*density ripples*) of expanding 1D quasi-condensates. The fast frame-transfer readout has also been used to image successively atoms in the two hyperfine states $F = 2$ (without repumper) and $F = 1$ (with repumper), which would be necessary for experiments with internal states of a BEC (see Sect. 3.1.2.1).

Note that it cannot be used to image the matter-wave interference patterns obtained from releasing a BEC from a horizontal double well (see Sect. 3.2.1) since the fringes, which are parallel to the (y, z) plane, are integrated out (see Fig. 2.16).

2.3.1.1 Atom Number Calibration by Saturation Absorption Imaging

As we will see in Sect. 3.4.3, precise number-squeezing measurements imply a correct estimation of the absolute atom number in our BECs. So far, N can only be inferred from absorption pictures. For this reason, it is absolutely necessary to characterize our absorption imaging system to obtain a reliable estimation of N.

We followed the approach proposed in Ref. [78], comparing the optical density of identical atomic samples measured at different intensities, well below and above saturation. At resonance, the photon scattering rate of a two-level atom reads

$$\dot{N}_{\mathrm{ph}} = \frac{\Gamma}{2} \frac{I/I_{\mathrm{sat}}}{1 + I/I_{\mathrm{sat}}}, \tag{2.38}$$

where Γ is the natural line width of the optical transition. For the optical transitions of the D2 line of ^{87}Rb, $\Gamma = 2\pi \times 6.07$ MHz [35]. The saturation intensity I_{sat} is connected to the resonant cross section σ_0 through

$$I_{\mathrm{sat}} = \Gamma \frac{\hbar\omega}{\sigma_0}. \tag{2.39}$$

To maximize the absorption signal, we chose to work in the configuration yielding the highest cross section, namely by using σ^+ polarized light to address the cycling transition $F = 2, m_{\mathrm{F}} = 2 \leftrightarrow F' = 3, m_{\mathrm{F}} = 3$. For this transition, $\sigma_0 = 2.91 \times 10^{-9}\,\mathrm{cm}^2$ and $I_{\mathrm{sat}} = 1.67\,\mathrm{mW/cm}^2$ [35]. Note that to access this transition, we must first repump the atoms (see Sect. 2.1.5) from $F = 1$ to $F' = 2$. The repumper light,

which is superimposed to the path of the imaging beam, is shone for ∼200 μs right before the imaging pulse.

In practice, however, the actual cross section is likely to be smaller than this value, depending on the exact configuration of the beam direction, polarization and the orientation of the magnetic field defining the quantization axis. To ensure that the atoms experience a σ^+ polarization, we use the small Bias coil (see Sect. 2.1.2) to apply a uniform magnetic field parallel to the optical axis (see Ref. [1]). Nevertheless, besides the imperfect alignment of the quantization field with respect to the optical axis, transient pumping effects are also expected to slightly reduce the effective cross section.

Following Ref. [78], we take into account the specific configuration of our absorption imaging by defining an effective cross section

$$\sigma_{\text{eff}} = \frac{\sigma_0}{\alpha} \tag{2.40}$$

with $\alpha \geq 1$ and the corresponding effective saturation intensity $I_{\text{sat}}^{\text{eff}} = \alpha I_{\text{sat}}$.

From the scattering rate (2.38), we can express the attenuation of a laser beam passing through an atomic cloud. After it has traveled through an infinitesimal distance dx in a cloud of density $n(\vec{r})$, the intensity of the imaging beam drops by

$$\mathrm{d}I = -\sigma_{\text{eff}} \frac{I}{1 + I/I_{\text{sat}}^{\text{eff}}} n(\vec{r}) \mathrm{d}x. \tag{2.41}$$

Integrating Eq. (2.41), we can express the optical density (OD) $\sigma_0 \tilde{n}$ as the sum of two terms:

$$\sigma_0 \tilde{n}(y, z) = \underbrace{\alpha \ln\left(\frac{I_{\text{i}}}{I_{\text{f}}}\right)}_{\log} + \underbrace{\frac{I_{\text{i}} - I_{\text{f}}}{I_{\text{sat}}^0}}_{\text{sat}}, \tag{2.42}$$

where I_i and I_f are respectively the intensity of the imaging beam before and after propagation through the atomic cloud. Far below the saturation intensity ($I_i \ll I_{\text{sat}}$), the logarithmic term dominates. This is the regime where most absorption imaging systems are operated. The column density is given by the Beer-Lambert law

$$\tilde{n}(y, z) = \sigma_{\text{eff}} \ln\left(\frac{I_i}{I_f}\right), \tag{2.43}$$

which has the important property that $\tilde{n}$, and hence the total atom number $N = \int\int \tilde{n} \mathrm{d}y \mathrm{d}z$ do not depend on the intensity of the imaging beam, provided it is sufficiently small.[17] However, it depends linearly on α, meaning that the atom number computed by absorption might be systematically underestimated when using the theoretical value σ_0 of the resonant cross section.

[17] Typically, this is true as long as $I \lesssim I_{\text{sat}}/10$.

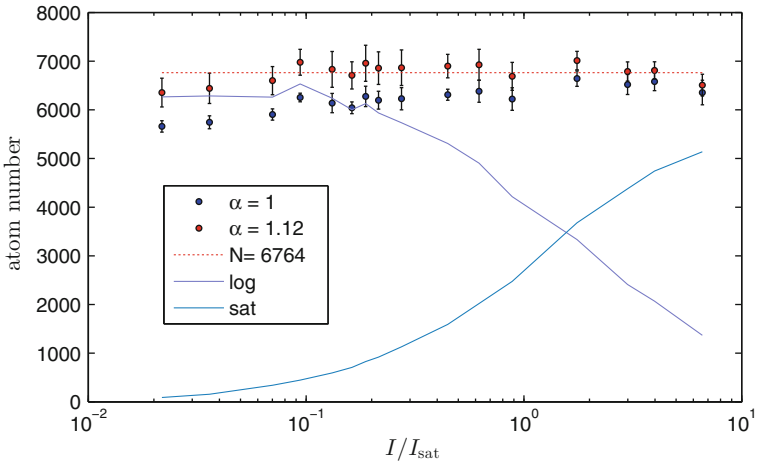

Fig. 2.18 Calibration of the absolute atom number in absorption. Measured atom number N in a BEC for different imaging beam intensities. For each intensity, the atom number was computed using Eq. (2.42). *Black points* atom number assuming $\alpha = 1$. *Red points* atom number corrected for $\alpha = 1.12$, in order to ensure a constant N regardless of I/I_{sat} (note that the points corresponding to the two lowest intensities, for which the pictures were very noisy, were not used to estimate α). *Continuous lines* logarithmic (*lavender blue*) and saturation (*medium turquoise*) terms (the logarithmic term has been computed for $\alpha = 1.12$). Both contributions are equal for $I = I_{\mathrm{sat}}^{\mathrm{eff}}$

The second term becomes dominant above saturation, i.e. when $I_i, I_f \gg I_{\mathrm{sat}}$. It does not depend on the effective cross section, because if all the atoms are saturated, their scattering rate is simply equal to $\Gamma/2$.

The method proposed in Ref. [78] consists in inferring α from absorption pictures of identical atomic clouds taken at different intensities, spanning a large range below and over I_{sat}. It relies on the assumption that (a) the atom number of all the observed atomic samples is the same, (b) the correction factor α is independent on the intensity of the probe beam. While the first assumption depends on the atom number stability of the experiment, which for us is of the order of 10 %, the second one was checked within our group by solving the optical Bloch equations for different imaging configuration close to ours.

We calibrated our absorption imaging system by taking images of a BEC with ∼6000 atoms at different intensities ranging from 0.02 I_{sat} to 8 I_{sat}. The number of scattered photons N_{ph} was kept approximately constant by adjusting the imaging pulse duration. We also checked experimentally that no significant Doppler shift was reducing the effective cross section even for the largest number of photons ($N_{\mathrm{ph}} \approx 300$).[18]

Figure 2.18 shows an example of the atom numbers computed with the full Eq. (2.42). Assuming $\alpha = 1$ (black points), we observed that the computed N was slightly increasing with increasing intensity, indicating that the logarithmic term in Eq. (2.42) was underestimated. Repeating the measurement for different values of

[18] It needs approximately 350 scattered photons for a ^{87}Rb atom to be Doppler-shifted by $\Gamma/2$.

N_{ph}, we found that the values of α ensuring a constant atom number (red points) was lying between 1.05 and 1.15. Furthermore, independent measurements of the axial Thomas-Fermi radius of a trapped condensate (see Sect. 1.1.3.3.) confirmed that we can exclude underestimating the atom number by more than 20 %.

2.3.2 *Fluorescence Imaging System (Light Sheet)*

Most of the data presented in the next chapters has been acquired with our fluorescence imaging system [1, 18, 19]. It is aligned along the vertical y-axis to image atoms in the horizontal (x, z) plane. It consists of a thin (waist radius: 20 μm) horizontal "sheet" of resonant (or slightly red-detuned) laser light located roughly 1 cm below the atom chip. When atoms are released from the trap, they expand and fall through the *light sheet* (LS) after a ∼46 ms tof. Each atom typically scatters hundreds of photons during the ∼100 μs it spends in the LS. A small fraction (around 2 %) of the fluorescent light is captured by an objective located below the vacuum chamber, and detected by an electron multiplying CCD camera[19] (EMCCD), yielding a typical sensitivity of $\bar{p} = 15$ detected photons per atom on average.

The LS is created by superimposing two identical counter-propagating laser beams, each of them coupled out of an optical fiber outside the chamber and sent through a cylindrical lens to obtain a highly anisotropic "flat" sheet of light (waist in horizontal direction: 4.5 mm). The optical axis of the LS is rotated by 45° with respect to the x and z-axis. A lin-⊥-lin polarization configuration was chosen to avoid creating an intensity grating, resulting in a polarization grating perpendicular to the optical axis. The total optical power (a few μW) can be adjusted to tune $\bar{p}$. It is actively stabilized against slow drifts by sampling a fraction of the optical power and readjusting the AOM amplitude accordingly every second experimental cycle, i.e. once per minute.

The custom objective [1] was sized in such a way that the geometric spot size and the diffraction limit remain smaller than the object space camera pixel size ($4 \times 4\,\mu\mathrm{m}^2$) over the whole field of view ($2 \times 2\,\mathrm{mm}^2$). An advantage of the LS configuration is that the depth of field can be matched to the thickness of the LS. This allows imaging thermal clouds after long tofs, which are generally larger than the depth of field set by our relatively high NA of 0.34 and would otherwise look blurred. The vertical position of the LS determines the tof. It can be adjusted by means of a translation stage, but changing the tof implies refocussing the optics, so that in practice, conversely to the absorption imaging system, we have to work with a fixed tof (46 ms), although we can adjust the duration of the LS pulse to image slices of the atomic cloud [21]. Imaging several slices of the same atomic cloud should be in principle possible, but is currently limited by the readout speed of the camera.

Currently, the main factor limiting the resolution of our fluorescence imaging system is the diffusion of the atoms in the LS [18]. The atoms perform a random

[19] Andor iXon+ 897.

walk in momentum space due to the stochastic absorption and re-emission events. This result in a real-space spot size for the fluorescence signal coming from each atom of typically 10 μm rms size, whereby the shape of the anisotropic fluorescence pattern depends on the detail of the scattering events.

The main asset of our fluorescence imaging system is its high sensitivity together with a high dynamical range [18], allowing us to detect single atoms as well as dense BECs. For each atom crossing the LS, we detect on average a number of photons sufficiently large so that the probability of not detecting an atom can be made vanishingly small. The mean number of detected photons per atom $\bar{p}$ can be increased by increasing the LS intensity, at the expense of the spatial resolution. We usually worked with $\bar{p} \approx 15$. Together with an extremely low background noise (the CCD chip is thermoelectrically cooled down to $-90\,^{\circ}\mathrm{C}$), our single-atom sensitivity has been a crucial condition to detect strong number squeezing [12, 14], as will be detailed in Sect. 3.2.2.2. It should be noted however that single-atom sensitivity does not mean the ability to resolve atoms in dense clouds, because of our limited resolution. Nevertheless, high signal-to-noise ratio associated with a relatively long tof are particularly advantageous to probe the high-k tails of the momentum distribution of thermal clouds and BECs, and has allowed studying the emission of high-momentum correlated atom pairs [12, 79].

The LS imaging system is oriented as to image the atoms from below, which is well-suited to image matter-wave interference patterns emerging from the recombination of a horizontally split condensate (see Sect. 3.2.1). In particular, it allowed probing the spatial phase correlations of a 1D BJJ [11]. It was also used to demonstrate Hanbury Brown and Twiss (HBT) correlations across the BEC threshold [21].

2.3.2.1 Calibration of Fluorescence Picture

In an EMCCD camera, each photon impinging on a pixel of the CCD chip is converted into a primary electron, which is amplified to a large number (up to about 1000) of secondary electrons. To calibrate the raw fluorescence picture, the gain of the electron multiplying unit is calibrated from a second picture taken immediately afterward, but without light. The second picture hence only contains technical noise, which is essentially due to clock-induced charges, i.e. charges created before the amplification process and therefore indistinguishable from real photons. Nevertheless, since the EM amplification is a stochastic process, the distribution of counts per pixel in the calibration picture can be fitted to retrieve the amplification gain (see Fig. 2.19, left pannel) [19]. It also provides information on the background level and the additional noise added by the readout stage. The fitted values are used to compute the processed fluorescence picture (in photon number/pixel) from the raw picture. An important consequence from the stochastic amplification is that it adds extra shot noise: the variance of the signal on a camera pixel with on average $\bar{s}$ photons is two times $\bar{s}$ (see Sect. 3.4.3.1).

An additional background contribution is caused by stray light from the LS beams. When working with cold condensates well-located in the center of the picture, this

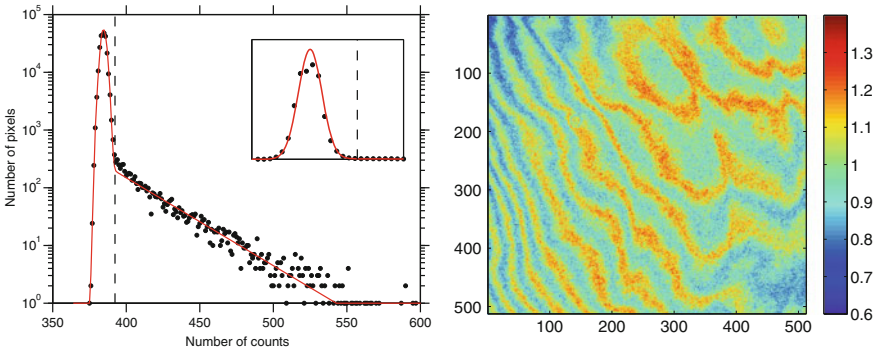

Fig. 2.19 Calibration of the fluorescence pictures. *Left* Taken from Ref. [19]. Distribution of the number of counts per pixel in a single image acquired without any light. The detected signal is only due to CIC. The continuous line is a fit of the distribution (see Ref. [19] for the fit model) allowing to extract the EM gain, the baseline and the readout noise. The *dashed line* marks the threshold of the readout cutoff. The *inset* shows the same distribution in linear scale. *Right* Etaloning. Reflections between the nearly parallel front and back surface of the narrow, back-illuminated CCD chip interfere, causing distortions of the images. Since it is constant over time, etaloning can be characterized from averaging hundreds of images of a hot thermal cloud to ensure uniform illumination, and accounted for as a position-dependent gain factor

usually uniform background can be calibrated from the edges of the images and subtracted. Another, non-uniform, contribution is due to etaloning, i.e. the interference of coherent light on the CCD chip acting as a non uniform Fabry-Perot etalon. While this does not affect significantly the signal integrated over a sufficiently large area, it leads to local distortions of the image. It can be highlighted by averaging hundreds of pictures of a sufficiently hot thermal cloud (to ensure a uniform illumination), see Fig. 2.19. Fortunately, as it doesn't change over time, it can be corrected for, for example to fit the profile of a cloud.

So far, the absolute column density (in atom/pix) cannot be easily deduced from the fluorescence pictures only, although alternative schemes based on the correlation properties of the fluorescence signal are currently being investigated. The average number of detected photons per atom $\bar{p}$ is hence inferred from imaging a series of (typically 20) condensates prepared in the same conditions, alternating between fluorescence and absorption imaging. It yields an uncertainty on $\bar{p}$ of the order of 10 %.

2.4 Conclusion of the Experimental Part

In this chapter, we have presented the apparatus on which the experiments presented in this thesis have been conducted. The main features of our compact ^{87}Rb BEC machine are

- the atom chip, which enable the creation of elongated magnetic traps with transverse frequencies in the kHz range and longitudinal frequencies between 10 and 20 Hz,
- the possibility to apply rf-dressing to manipulate the transverse confinement and realize a tunable double-well geometries,
- a light sheet fluorescence imaging system which allows probing the BECs with single-atom sensitivity.

References

1. R. Bücker, *Twin-atom beam generation in a one-dimensional Bose gas*. Ph.D. thesis, Vienna University of Technology, 2013
2. P. Krüger, *Coherent matter waves near surfaces*. Ph.D. thesis, Heidelberg, 2004
3. S. Wildermuth, *One-dimensional Bose-Einstein condensates in micro-traps*. Ph.D. thesis, Heidelberg, 2005
4. H. Gimpel, *Magnetische Oberflächenfallen für Atom-Interferomete*. Diploma thesis, Heidelberg, 2002
5. C. Becker, *Eine neuartige magneto-optische Falle für Atomchip-Experimente.* Diploma thesis, Heidelberg, 2002
6. S. Haupt, *Setup of a new experiment with ultracold 87Rb Atoms: towards quantum information processing on an atom chip*. Ph.D. thesis, Heidelberg, 2003
7. S. Hofferberth, *Experiments with ultracold atoms and Bose-Einstein condensated in microtraps near surfaces*. Diploma thesis, Heidelberg, 2004
8. T. Schumm, *Bose-Einstein condensates in magnetic double well potentials*. Ph.D. thesis, Université Paris 11, 2005
9. S. Hofferberth, *Coherent manipulation of Bose-Einstein condensates with rf adiabatic potentials*. Ph.D. thesis, Heidelberg, 2007
10. T. Betz, *Phase correlations of coupled one-dimensional Bose gases*. Ph.D. thesis, Vienna University of Technology, 2011
11. T. Betz, S. Manz, R. Bücker, T. Berrada, Ch. Koller, G. Kazakov, I. Mazets, H.-P. Stimming, A. Perrin, T. Schumm, J. Schmiedmayer, Two-point phase correlations of a one-dimensional Bosonic Josephson junction. Phys. Rev. Lett. **106**(2) (2011)
12. R. Bücker, J. Grond, S. Manz, T. Berrada, T. Betz, C. Koller, U. Hohenester, T. Schumm, A. Perrin, J. Schmiedmayer, Twin-atom beams. Nat. Phys. **7**(8), 608–611 (2011)
13. R. Bücker, T. Berrada, S. van Frank, J.-F. Schaff, T. Schumm, J. Schmiedmayer, G. Jäger, J. Grond, U. Hohenester, Vibrational state inversion of a Bose-Einstein condensate: optimal control and state tomography. J. Phys. B: At. Mol. Opt. Phys. **46**(10), 104012 (2013)
14. T. Berrada, S. van Frank, R. Bücker, T. Schumm, J.-F. Schaff, J. Schmiedmayer, Integrated Mach-Zehnder interferometer for Bose-Einstein condensates. Nat. Commun. **4**, 2077 (2013)
15. S. Groth, *Development, fabrication, and characterisation of atom chips*. Ph.D. thesis, University of Heidelberg, 2006
16. S. Manz, *Density correlations of expanding one-dimensional Bose gases*. Ph.D. thesis, TU Vienna, 2011
17. M. Trinker, S. Groth, S. Haslinger, S. Manz, T. Betz, S. Schneider, I. Bar-Joseph, T. Schumm, J. Schmiedmayer, Multilayer atom chips for versatile atom micromanipulation. Appl. Phys. Lett. **92**(25), 254102 (2008)
18. R. Bücker, *Fluorescence imaging of ultracold atoms*. Diploma thesis, Heidelberg, 2008
19. R. Bücker, A. Perrin, S. Manz, T. Betz, C.H. Koller, T. Plisson, J. Rottmann, T. Schumm, J. Schmiedmayer, Single-particle-sensitive imaging of freely propagating ultracold atoms. New J. Phys. **11**(10), 24 (2009)

20. S. Manz, R. Bücker, T. Betz, C. Koller, S. Hofferberth, I.E. Mazets, A. Imambekov, E. Demler, A. Perrin, J. Schmiedmayer, T. Schumm, Two-point density correlations of quasicondensates in free expansion. Phys. Rev. A **81**(3), 031610 (2010)
21. A. Perrin, R. Bücker, S. Manz, T. Betz, C. Koller, T. Plisson, T. Schumm, J. Schmiedmayer, Hanbury Brown and Twiss correlations across the Bose Einstein condensation threshold. Nat. Phys. **8**(3), 195–198 (2012)
22. C. Koller, *Towards the realization of hybrid quantum systems*. Ph.D. thesis, Vienna University of Technology, 2012
23. T. Plisson, *Coherent manipulation of Bose-Einstein condensates with microwave and radio frequency fields*. Diploma thesis, Télécom Paristech, 2009
24. M. Brajdic, *Entwicklung einer Computersteuerung und ihre Anwendung in einem Experiment zur vereinfachten Bose-Einstein Kondensation in einer Oberflächen- falle*. Diploma thesis, Heidelberg, 2003
25. W. Rohringer, *Stochastic optimization in an ultracold atom experiment*. Diploma thesis, Vienna University of Technology, 2008
26. W. Rohringer, R. Bücker, S. Manz, T. Betz, C. Koller, M. Göbel, A. Perrin, J. Schmiedmayer, T. Schumm, Stochastic optimization of a cold atom experiment using a genetic algorithm. Appl. Phys. Lett. **93**(26), 264101 (2008)
27. R. Folman, P. Krüger, J. Schmiedmayer, J. Denschlag, C. Henkel, Microscopic atom optics: from wires to an atom chip. Adv. At. Mol. Opt. Phys. **48**, 263–356 (2002)
28. S. Wildermuth, P. Krüger, C. Becker, M. Brajdic, S. Haupt, A. Kasper, R. Folman, J. Schmiedmayer, Optimized magneto-optical trap for experiments with ultracold atoms near surfaces. Phys. Rev. A **69**(3), 030901 (2004)
29. A. Haase, D. Cassettari, B. Hessmo, J. Schmiedmayer, Trapping neutral atoms with a wire. Phys. Rev. A **64**(4), 043405 (2001)
30. S. Schneider, A. Kasper, Ch. vom Hagen, M. Bartenstein, B. Engeser, T. Schumm, I. Bar-Joseph, R. Folman, L. Feenstra, J. Schmiedmayer, Bose-Einstein condensation in a simple microtrap. Phys. Rev. A **67**(2), 023612 (2003)
31. M. Wilzbach, *Aufbau eines Experiments zur miniaturisierten und integrierten Detektion neutraler Atome*. Diploma thesis, Heidelberg, 2002
32. R. Bücker, T. Berrada, S. van Frank, J.-F. Schaff, T. Schumm, J. Schmiedmayer, G. Jäger, J. Grond, U. Hohenester, Vibrational state inversion of a Bose-Einstein condensate: optimal control and state tomography, arXiv:1212.4173. Accessed Dec 2012
33. S. van Frank, A. Negretti, T. Berrada, R. Bücker, S. Montangero, J.-F. Schaff, T. Schumm, T. Calarco, J. Schmiedmayer, Interferometry with non-classical motional states of a Bose-Einstein condensate, p. 7, Feb 2014
34. J.F. Scharf, Eine Partitur der atomaren Bewegung. Wiener Zeitung, 2012
35. D.A. Steck, Rubidium 87 D Line Data. Technical report, 2008
36. C. Cohen-Tannoudji, Atomes ultrafroids - Piègeage non dissipatif et refroidissement évaporatif, in *Notes de Cours au Collège de France*, p. II (1996)
37. E. Burt, R. Ghrist, C. Myatt, M. Holland, E. Cornell, C. Wieman, Coherence, correlations, and collisions: what one learns about Bose-Einstein condensates from their decay. Phys. Rev. Lett. **79**(3), 337–340 (1997)
38. J. Söding, D. Guéry-Odelin, P. Desbiolles, F. Chevy, H. Inamori, J. Dalibard, Three-body decay of a rubidium Bose-Einstein condensate. Appl. Phys. B: Lasers Opt. **69**(4), 257–261 (1999)
39. J. Schmiedmayer, Guiding and trapping a neutral atom on a wire. Phys. Rev. A **52**(1), R13–R16 (1995)
40. J. Reichel, W. Hänsel, T. Hänsch, Atomic micromanipulation with magnetic surface traps. Phys. Rev. Lett. **83**(17), 3398–3401 (1999)
41. R. Folman, P. Krüger, D. Cassettari, B. Hessmo, T. Maier, J. Schmiedmayer, Controlling cold atoms using nanofabricated surfaces: atom chips. Phys. Rev. Lett. **84**(20), 4749–4752 (2000)
42. W. Hänsel, P. Hommelhoff, T.W. Hänsch, J. Reichel, Bose-Einstein condensation on a microelectronic chip. Nature **413**(6855), 498–501 (2001)

43. H. Ott, J. Fortagh, G. Schlotterbeck, A. Grossmann, C. Zimmermann, Bose-Einstein condensation in a surface microtrap. Phys. Rev. Lett. **87**(23), 230401 (2001)
44. J. Reichel, V. Vuletic, *Atom Chips* (Wiley, New York, 2010)
45. T.H. Bergeman, P. McNicholl, J. Kycia, H. Metcalf, N.L. Balazs, Quantized motion of atoms in a quadrupole magnetostatic trap. J. Opt. Soc. Am. B, **6**(11), 2249 (1989)
46. T. Schumm, Atom chips in the real world: the effects of wire corrugation. EPJD **32**, 171–180 (2005)
47. S. Groth, P. Krüger, S. Wildermuth, R. Folman, T. Fernholz, J. Schmiedmayer, D. Mahalu, I. Bar-Joseph, Atom chips: fabrication and thermal properties. Appl. Phys. Lett. **85**(14), 2980 (2004)
48. J. Estève, C. Aussibal, T. Schumm, C. Figl, D. Mailly, I. Bouchoule, C. Westbrook, A. Aspect, Role of wire imperfections in micromagnetic traps for atoms. Phys. Rev. A **70**(4), 043629 (2004)
49. P. Krüger, L. Andersson, S. Wildermuth, S. Hofferberth, E. Haller, S. Aigner, S. Groth, I. Bar-Joseph, J. Schmiedmayer, Potential roughness near lithographically fabricated atom chips. Phys. Rev. A **76**(6), 063621 (2007)
50. J.-B. Trebbia, C. Garrido, Alzar, R. Cornelussen, C. Westbrook, I. Bouchoule, Roughness suppression via rapid current modulation on an atom chip. Phys. Rev. Lett. **98**(26), 263201 (2007)
51. R. Grimm, M. Weidemüller, Y.B. Ovchinnikov, Optical dipole traps for neutral atoms. Adv. At. Mol. Opt. Phys. **42**, 95–170 (2000)
52. H. Perrin, *Adiabatic Potentials*, Lecture on Adiabatic Potentials, Les houche edition, 2013
53. O. Zobay, B. Garraway, Two-dimensional atom trapping in field-induced adiabatic potentials. Phys. Rev. Lett. **86**(7), 1195–1198 (2001)
54. Y. Colombe, E. Knyazchyan, O. Morizot, B. Mercier, V. Lorent, H. Perrin, Ultracold atoms confined in rf-induced two-dimensional trapping potentials. Europhys. Lett. (EPL) **67**(4), 593–599 (2004)
55. I. Lesanovsky, T. Schumm, S. Hofferberth, L. Andersson, P. Krüger, J. Schmiedmayer, Adiabatic radio-frequency potentials for the coherent manipulation of matter waves. Phys. Rev. A **73**(3), 033619 (2006)
56. O. Morizot, Y. Colombe, V. Lorent, H. Perrin, B. Garraway, Ring trap for ultracold atoms. Phys. Rev. A **74**(2), 023617 (2006)
57. P.W. Courteille, B. Deh, J. Fortágh, A. Günther, S. Kraft, C. Marzok, S. Slama, C. Zimmermann, Highly versatile atomic micro traps generated by multifrequency magnetic field modulation. J. Phys. B: At. Mol. Opt. Phys. **39**(5), 1055–1064 (2006)
58. T. Schumm, S. Hofferberth, L.M. Andersson, S. Wildermuth, S. Groth, I. Bar-Joseph, J. Schmiedmayer, P. Krüger, Matter-wave interferometry in a double well on an atom chip. Nat. Phys. **1**(1), 57–62 (2005)
59. S. Hofferberth, I. Lesanovsky, B. Fischer, J. Verdu, J. Schmiedmayer, Radiofrequency-dressed-state potentials for neutral atoms. Nat. Phys. **2**(10), 710–716 (2006)
60. G.-B. Jo, J.-H. Choi, C.A. Christensen, Y.-R. Lee, T.A. Pasquini, W. Ketterle, D.E. Pritchard, Matter-wave interferometry with phase fluctuating Bose-Einstein condensates. Phys. Rev. Lett. **99**(24), 240406 (2007)
61. F. Baumgärtner, R.J. Sewell, S. Eriksson, I. Llorente-Garcia, J. Dingjan, J.P. Cotter, E.A. Hinds, Measuring energy differences by BEC interferometry on a chip. Phys. Rev. Lett. **105**(24), 243003 (2010)
62. L. LeBlanc, A. Bardon, J. McKeever, M. Extavour, D. Jervis, J. Thywissen, F. Piazza, A. Smerzi, Dynamics of a tunable superfluid junction. Phys. Rev. Lett. **106**(2) (2011)
63. S. Hofferberth, I. Lesanovsky, B. Fischer, T. Schumm, J. Schmiedmayer, Non-equilibrium coherence dynamics in one-dimensional Bose gases. Nature **449**(7160), 324–327 (2007)
64. M. Gring, M. Kuhnert, T. Langen, T. Kitagawa, B. Rauer, M. Schreitl, I. Mazets, D. Adu, Smith, E. Demler, J. Schmiedmayer, Relaxation and prethermalization in an isolated quantum system. Science (New York, N.Y.) **337**(6100), 1318–1322 (2012)

65. K. Merloti, R. Dubessy, L. Longchambon, A. Perrin, P.-E. Pottie, V. Lorent, H. Perrin, A two-dimensional quantum gas in a magnetic trap. New J. Phys. **15**(3), 033007 (2013)
66. J. Shirley, Solution of the Schrödinger equation with a Hamiltonian periodic in time. Phys. Rev. **138**(4B), B979–B987 (1965)
67. H. Perrin, *Spin and Fields*, Lecture on Adiabatic Potentials, Les houche edition, 2013
68. A. Martin, K. Helmerson, V. Bagnato, G. Lafyatis, D. Pritchard, rf Spectroscopy of trapped neutral atoms. Phys. Rev. Lett. **61**(21), 2431–2434 (1988)
69. I. Bloch, T. Hänsch, T. Esslinger, Atom laser with a cw output coupler. Phys. Rev. Lett. **82**(15), 3008–3011 (1999)
70. S. Hofferberth, B. Fischer, T. Schumm, J. Schmiedmayer, I. Lesanovsky, Ultracold atoms in radio-frequency dressed potentials beyond the rotating-wave approximation. Phys. Rev. A **76**(1), 013401 (2007)
71. J. van Es, S. Whitlock, T. Fernholz, A. van Amerongen, N. van Druten, Longitudinal character of atom-chip-based rf-dressed potentials. Phys. Rev. A **77**(6), 063623 (2008)
72. A. Robert, O. Sirjean, A. Browaeys, J. Poupard, S. Nowak, D. Boiron, C.I. Westbrook, A. Aspect, A Bose-Einstein condensate of metastable atoms. Science (New York, N.Y.) **292**(5516), 461–464 (2001)
73. T. Gericke, P. Würtz, D. Reitz, T. Langen, H. Ott, High-resolution scanning electron microscopy of an ultracold quantum gas. Nat. Phys. **4**(12), 949–953 (2008)
74. W. Ketterle, D.S. Durfee, D.M. Stamper-Kurn, Making, probing and understanding Bose-Einstein condensates, p. 90, Apr 1999
75. A. David, Smith, S. Aigner, S. Hofferberth, M. Gring, M. Andersson, S. Wildermuth, P. Krüger, S. Schneider, T. Schumm, J. Schmiedmayer, Absorption imaging of ultracold atoms on atom chips. Opt. Exp. **19**(9), 8471–8485 (2011)
76. M Gring, *Prethermalization in an isolated many body system*. Ph.D. thesis, Vienna University of Technology, 2012
77. T. Jacqmin, *Mesures de corrélations dans un gaz de bosons unidimensionnel sur puce*. Ph.D. thesis, Université Paris Sud, 2012
78. G. Reinaudi, T. Lahaye, Z. Wang, D. Guéry-Odelin, Strong saturation absorption imaging of dense clouds of ultracold atoms. Opt. Lett. **32**(21), 3143 (2007)
79. R. Bücker, U. Hohenester, T. Berrada, S. van Frank, A. Perrin, S. Manz, T. Betz, J. Grond, T. Schumm, J. Schmiedmayer, Dynamics of parametric matter-wave amplification. Phys. Rev. A **86**(1), 013638 (2012)

http://www.springer.com/978-3-319-27232-0

Interferometry with Interacting Bose-Einstein Condensates in a Double-Well Potential

Berrada, T.

2016, XIX, 229 p. 89 illus., 67 illus. in color., Hardcover
ISBN: 978-3-319-27232-0